Powder Technology 466 (2025) 121423

Contents lists available at ScienceDirect

Powder Technology

journal homepage: www.journals.elsevier.com/powder-technology

Characterization of thermal properties of ball-milled copper-graphene powder as feedstock for additive manufacturing

Hyunjong Lee [a,b,*], Davoud Jafari [b], Apostolos Koutsioukis [c], Valeria Nicolosi [c], Bernard J. Geurts [a], Wessel W. Wits [a,d]

[a] Mathematics of Multiscale Modeling and Simulation, Faculty EEMCS, University of Twente, P.O. Box 217, 7500 AE Enschede, The Netherlands
[b] Faculty of Engineering Technology, University of Twente, P.O. Box 217, 7500 AE Enschede, The Netherlands
[c] School of Chemistry, CRANN and AMBER Research Centres, Trinity College Dublin, College Green, Dublin D02 PN40, Ireland
[d] NLR – Royal Netherlands Aerospace Centre, Marknesse, The Netherlands

HIGHLIGHTS

- Thermal conductivity of copper-graphene powder beds is reported for the first time.
- A novel ball-milled copper-graphene feedstock is developed for additive manufacturing.
- A reliable steady-state method is developed for powder bed thermal characterization.
- Particle morphology significantly alters the powder thermal conductivity.
- Impact of graphene on powder bed thermal properties is studied using thermal models.

GRAPHICAL ABSTRACT

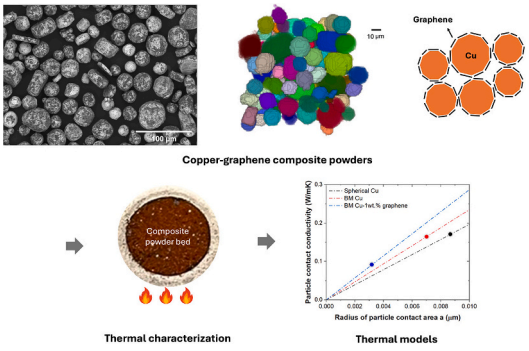

ARTICLE INFO

Keywords:
Additive manufacturing
3D printing
Powder bed fusion
Metal-matrix composites
Graphene
Ball milling
Thermal conductivity
Thermal management
Heat transfer
Powder bed properties
Microstructure
2D materials

ABSTRACT

Thermal properties of novel powder feedstocks, such as copper-graphene, remain largely unexplored despite their importance in heat dissipation and manufacturability in powder bed-based additive manufacturing (AM) processes. Therefore, this study characterizes the thermal properties of copper, graphene, and copper-graphene composite powder beds produced via ball milling (BM) using differential scanning calorimetry (DSC). Results reveal that BM reduces the effective thermal conductivity (ETC) up to ~44 % for copper and ~ 70 % for graphene powders. This is primarily due to the changes in particle morphology and the resulting modification in particle aspect ratio. Similar observations apply if copper and graphene are mixed, with up to ~33 % reduction in ETC. This reduction is however attributed to the surface modification of the graphene-coated copper particle, providing a smaller contact radius compared to spherical copper and BM copper. This results in less effective heat conduction across the composite powder particle. Additionally, heat conduction through powder beds is analyzed by comparing the measured data with established thermal models, including Maxwell-Garnett approximation and thermal resistance network models. We demonstrate that microstructural modifications in powder beds, driven by particle morphology and surface modifications, substantially impact the ETC of copper-graphene composite powder beds.

* Corresponding author at: University of Twente, Building Carre, room C3730, P.O. Box 217, 7500 AE Enschede, the Netherlands.
E-mail address: h.lee@utwente.nl (H. Lee).

https://doi.org/10.1016/j.powtec.2025.121423
Received 10 May 2025; Received in revised form 15 July 2025; Accepted 17 July 2025
Available online 19 July 2025
0032-5910/© 2025 The Authors. Published by Elsevier B.V. This is an open access article under the CC BY license (http://creativecommons.org/licenses/by/4.0/).

1. Introduction

Thermal characterization of powder feedstock is crucial as their processing, e.g., through additive manufacturing (AM), is influenced by the thermal properties of these powders. For instance, the quality of final products fabricated by laser-based powder bed fusion (L-PBF) AM is influenced by the effective thermal conductivity (ETC) of the powder bed, as it affects the resulting heat dissipation efficiency [1,2]. Hofmann et al. and Wits et al. reported that the influence of powder bed ETC on part quality is prominent when printing overhanging structure, as heat dissipation required for successful fabrication happens mostly through the powder bed [2,3].

Furthermore, the AM part quality can be enhanced knowing the thermal properties of the powder beds, as illustrated via the quality prediction of process and parts using thermal modeling and simulation [4–6]. This is particularly important when processing novel materials such as copper-graphene powder feedstocks with yet unknown process parameters. Accurate measurements of ETC in powder beds are however challenging due to the difficulties in handling powders and the large number of involved parameters, including packing density [7], material compositions [8], type of atmosphere [9], and pressure [9]. Moreover, characterizing composite powder beds (e.g., copper-graphene) is particularly complicated due to the uncertain interactions between the material compositions and their microstructural features, such as morphology, particle size, and the spatial distribution of graphene. Up to date, there has not been an in-depth study on the ETC of composite powder beds, particularly for the system of copper-graphene composite powder bed.

In this paper, we extend the differential scanning calorimetry (DSC) method to measure the ETC of copper-graphene powder beds [10–12]. In fact, we have modified the DSC method to be a steady-state thermal conductivity measurement platform, by measuring the heat input, Q, and the temperature gradient, ΔT, across the powder bed. As a result, the relationship between the various factors and the resulting ETC can be analyzed and correlated to the morphology, particle size distribution (PSD), and distribution of graphene observed by electron microscopy. The ETC of copper-graphene powders can be utilized to optimize powder bed-based AM processes and can provide a guideline for preparing composite powders for AM.

Copper-graphene, a type of relatively new material composites, employs the inclusion of 2D materials into metal-matrix composites (2DMMCs). These new composites have achieved breakthroughs in both mechanical [13] and thermal properties [14] through the addition of 2D materials, such as graphene, into the metallic matrix [15]. Copper-graphene is one of the most promising candidates for heat transfer applications [16], due to the extremely high thermal conductivity of graphene, ranging from 3000 W/mK to 5000 W/mK [17], excellent mechanical strength of 130 GPa and mechanical stiffness of 1 TPa, along with the benefits arising from the mechanical ductility of the copper matrix. Indeed, Chu et al. demonstrated a high thermal conductivity of 525 W/mK through the addition of 35 vol% graphene in a copper matrix via sintering [18], while Li et al. enhanced the thermal conductivity of copper to 638 W/mK using electrodeposition coating of graphene onto the copper [19].

The degree to which the CTE of copper-graphene can also be tailored to design requirements is important. Such tailoring can be also achieved by varying the amount of graphene in the copper matrix [20], thereby expanding the applicability of copper-graphene for heat transfer systems. However, the realization of these excellent potentials of copper-graphene on an industrial scale through conventional manufacturing techniques, such as sintering, electrodeposition, and chemical vapor deposition has been limited so far.

To address this issue, newly emerging fabrication techniques such as AM [21,22] offer advantages in scalability, geometric flexibility, rapid prototyping, and microstructure control, suggesting a pathway for integrating graphene into three-dimensional (3D) metal matrices [23]. Among AM techniques, powder-bed-based techniques such as powder bed fusion (PBF), hold promise for rapid fabrication with controlled microstructure [24,25].

Research into how the high potential of copper-graphene composites can be realized using AM is still in its early stages. Studies on thermal characterization of copper-graphene composite powders produced by various methods for AM are essential to ensure the stability of the AM process and the quality of the final parts. For this purpose, the entire chain from powder production and characterization to AM fabrication of the copper-graphene parts needs attention. Yet, limited studies have focused on characterizing copper-graphene composite powders for AM. Tidén et al. [26] produced copper-graphene oxide powders using wet-chemical processes, for L-PBF process. However, the electrical conductivity (~77.8 % of IACS; International Annealed Copper Standard) of copper with 0.3 wt% of graphene oxide was lower than that of commercially produced pure copper (~90 % of IACS). In addition, no in-depth study on how the powder characteristics of copper-graphene influence the properties of fabricated parts was presented. Calignano et al. [27] studied L-PBF of ball-milled copper-graphene composites, but characterization of the developed powder feedstock was not addressed. This reality highlights the necessity of the current study – research into the ETC of copper-graphene powder for AM processing.

Among several techniques for producing copper-graphene composite powders for AM, ball milling (BM) stands out due to its potential for large-scale production, cost-effectiveness, and eco-friendliness [28–30]. Moreover, the spatial distribution of graphene onto the copper particles can be controlled through the variation of BM parameters, such as milling time and speed, and the amount of graphene powder. The utilization of BM for copper-graphene powder production for AM may, however, also affect the microstructure and thermal properties of the resulting powder. Hence, careful assessment of BM copper-graphene powder for AM processes is required. Accordingly, we perform thermal characterization of BM copper-graphene composite powders, varying the graphene wt%, and considering the microstructural changes to quantify the influence of graphene addition on the ETC of composite powder beds.

The organization of this paper is as follows. For systematic characterization, in Section 2, the key features of the powder that can influence the thermal properties, such as microstructure and wt% of graphene, are discussed. Section 3 is dedicated to discussing the thermal characterization methodologies and experimental setup used for the powder characterization. In Section 4, the impact of BM on the thermal properties of copper, graphene, and copper-graphene composites is presented, including the impact of microstructural evolution during BM on the thermal properties. Finally, concluding remarks are collected in Section 5.

2. Relevance of powder characteristics for powder-bed-based additive manufacturing

Powder-bed-based AM of new materials, such as BM copper-graphene, requires careful consideration of powder characteristics, including thermal properties, microstructure, and graphene content (wt %). Each characteristic may affect another e.g., microstructural changes in BM copper-graphene powders can alter particle morphology, thereby affecting thermal properties. Alternatively, the addition of graphene to copper particles via BM could improve the thermal conductivity of individual particles, but its effect on the ETC of the powder bed remains unclear. Furthermore, BM may lead to unexpected changes in the PSD. Therefore, we aim to propose the ideal characteristics of BM copper-graphene powder feedstocks for AM and discuss the potential impact of each characteristic element on AM performance.

Since BM is known to cause particle deformation [28], achieving uniform incorporation of graphene without significant microstructural alteration is ideal. Thus, the optimal copper-graphene powder feedstocks are expected to exhibit a spherical morphology, a narrow size

distribution, and uniform graphene coverage. Accordingly, we focus on the following three aspects in characterizations: (1) microstructure of powders on scanning electron microscopy (SEM) scales, and (2) the amount of graphene (e.g., wt%), and (3) the resulting ETC of the powder bed. We will investigate these three aspects of in-house BM-prepared powders, particularly focusing on modifications caused by BM time. The motivation to focus on these three aspects is as follows:

2.1. Amount of graphene

The variation in graphene content with copper during BM can influence the surface coverage of the graphene and the thermal conductivity of individual particles. In powder-bed-based AM, both aspects have an impact on successful processability. First, the laser absorptivity of the powder can be altered by the graphene coating [31]. Second, the thermal conductivity of individual particles affect the heat dissipation rate [8]. However, the impact of graphene coating on thermal properties of powder beds is more complex. The structural anisotropy of graphene, such as its aspect ratio, which can be affected by BM, adds to the complexity of randomly mixed copper-graphene particles. Additionally, multiple heat conduction paths in the copper-graphene powder bed complicate ETC predictions. Moreover, the potential surface modification of copper particles by graphene introduces another factor to consider. Therefore, specifically, the impact of the graphene contents on the ETC of the powder bed is one of the key questions that needs to be addressed in this paper.

2.2. Microstructure

The microstructure of powder beds, such as morphology and PSD, significantly influences powder-bed-based AM processes. This includes the change in laser absorptivity and powder flowability of which the latter indicates the ability of powder to flow against cohesive forces. For instance, smaller powder particles, as expressed by an increased small-scale tail of the PSD, are beneficial for the laser absorptivity. This is because the laser light will be scattered more often by finer powder, which enhances the laser absorptivity [32]. On the other hand, larger powder particles, as seen by a large-scale tail of the PSD, can contribute to improving the powder's flowability by reducing the cohesive forces between powders. In addition, the morphology of the powder also influences the powder flowability [33], which in the end plays a role in the process stability and final quality of AM parts [34]. The influence of the PSD and the morphology of powders on the thermal properties of powder beds has not yet been studied experimentally. Numerical simulations have provided insights revealing that heat conduction paths can be affected by both PSD and morphology, which therefore have an impact on the ETC of powder beds [35,36]. Furthermore, the influence of a complex microstructure with two peaks in a (bi-modal) PSD and considerable morphological changes has not yet been studied experimentally, nor numerically.

2.3. Thermal properties

In AM processes such as L-PBF, various thermal factors influence the manufacturing process. This encompasses multiple heat transfer phenomena (e.g., heat conduction through the powder bed as well as through fabricated parts, convection, and radiation). The ETC of the powder bed, one of the key thermal properties, affects the printability of materials in both L-PBF [37] and e-beam PBF [1]. The heat dissipation rate during PBF processes is influenced by the ETC of the powder bed, e.g., high heat conduction within a powder bed can lead to efficient heat dissipation and less thermal stress, ensuring better quality of fabricated parts. Also, the thermal stability of the melt pool during PBF is influenced by the local ETC, even preventing fusion phenomena at very low ETC [1]. Therefore, accurate thermal characterization of powder beds is essential to optimize AM process parameters and to ensure process stability, particularly for novel complex composite powders such as copper-graphene.

Overall, the individual effects of 1. graphene contents, 2. microstructure and 3. thermal properties of the powder bed on AM are relatively evident; however, mutual influences of these properties on one other have not been extensively studied before. Therefore, the influence of powder microstructure and the wt% of graphene on the thermal properties of BM copper-graphene are the focus of this paper. The key hypothesis is that optimization of powder properties, taking specific requirements of a particular AM methodology into account, will enable the fabrication of the best possible parts.

3. Methods and experimental setup

Three powder types—pure copper, graphene, and copper-graphene composites produced by BM—are characterized for their morphology, PSD, ETC, packing density of the powder bed, and oxidation state to understand how each of these factors influences the thermal properties of the produced feedstock powders for AM. Fig. 1 outlines the characterization framework used for the systematic analysis.

Powder feedstocks with different compositions (i.e., wt% of graphene) are prepared by specific BM recipes, and their morphology is analyzed using SEM and micro-computed tomography (μ-CT) scanning. Subsequently, the PSD of the powder feedstock is extracted from image analysis of the obtained SEM images. Measuring the ETC of a packed powder bed is conducted in a crucible using an extended DSC method. The packing density of the powder samples is determined by the mass and volume of the powder in each of the samples. Lastly, the oxidation state of BM powder before and after the DSC measurements is analyzed using XPS, to isolate the influence of oxidation on the ETC. The detailed processes of each characterization method are individually discussed in Section 3.1 (Powder productions via BM), Section 3.2 (Powder morphology and PSD), Section 3.3 (Effective thermal conductivity measurements), and Section 3.4 (Oxidation state characterizations).

3.1. Copper, graphene, and copper-graphene powder productions via BM

In this section, materials and BM recipes for producing powder feedstock of copper, graphene, and copper-graphene composites are described.

To prepare the copper-based powders, including BM copper and copper-graphene powders, gas-atomized spherical copper powder (purity >99,95 %, SAFINA, Czech Republic) specifically designed for AM is utilized for the dry BM process. The initial powder size of copper starts with a PSD between 15 μm and 38 μm with an average D_{50} value of 22 μm. The BM process is performed using a standard planetary BM machine (PQ-N2 planetary ball mill, Across International, Australia) with two jars, filled with 5 mm stainless steel balls for the milling process, as shown in Fig. 2. The BM time for copper varies from 6 h to 12 h, and up to 24 h. This 6 h BM interval is chosen based on literature observations, which suggest that an appropriate BM time from 4 h to 8 h for copper-graphene production [38,39]. The production of BM-copper under the various BM times is carried out as we expect modifications in microstructural and thermal properties of powders caused by variations in BM time.

Graphene powder is produced by BM graphite powders (100 mesh particle sizes – corresponding to an average size of 149 μm, Sigma-Aldrich, USA) under the variation of BM time (6 h, 12 h, and 24 h), which will be used to adhere graphene layers onto the surface of copper powder particles in a second BM step. Copper-graphene powder is created by mixing copper and graphene powders, with the graphene content varying from 1 wt% to 3 wt%, 10 wt% and 20 wt% (each of them corresponds to 3.8 vol%, 10.9 vol%, 30.5 vol%, and 49.7 vol%). The variation in graphene content within the copper matrix is selected to study the effect of graphene wt% of copper-graphene on the thermal properties. Here, the appropriate BM time for mixing copper and

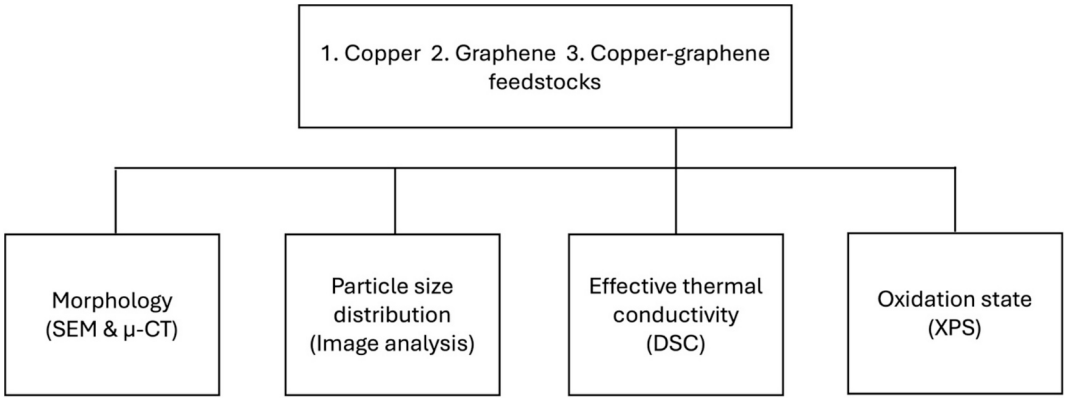

Fig. 1. Framework for the characterization of copper-graphene composite powder feedstocks. 1. Copper, 2. Graphene, 3. Copper-graphene feedstocks are sequentially characterized according to the proposed framework.

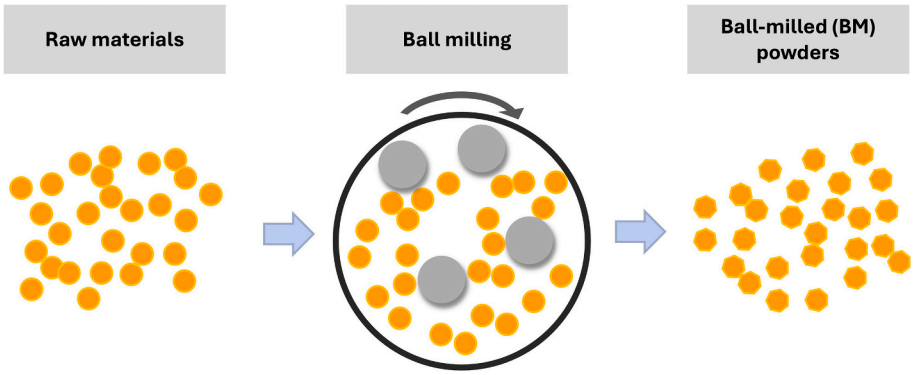

Fig. 2. Illustration of powder production using the ball milling (BM) process. Copper, graphene, and copper-graphene powders are produced via BM for microstructural and thermal characterization.

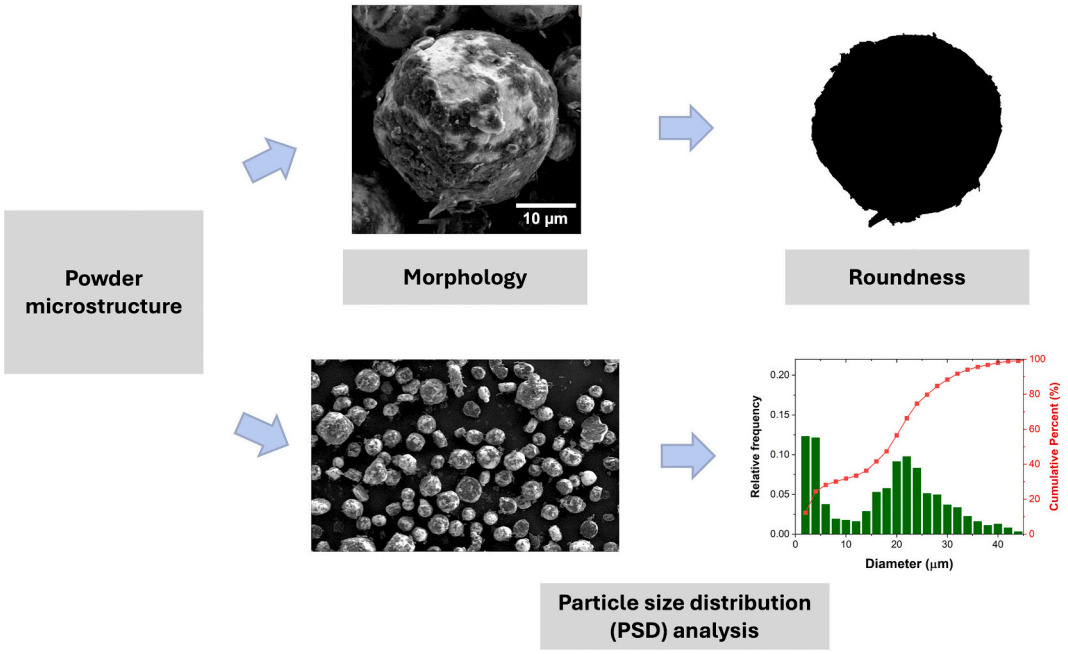

Fig. 3. Diagram for powder microstructure characterization, including morphology (e.g., roundness) and PSD using SEM imaging.

graphene will be selected based on the BM results of copper powders, which exhibit the highest ETC and a morphology suitable for AM.

3.2. Powder morphology and particle size distribution (PSD) analysis

Microstructure analysis of the powder is divided into two categories: 1. Morphology and 2. PSD. These factors may significantly influence the thermal properties of powder beds during AM processes. Powder morphology observation and PSD analysis are primarily characterized using SEM (Phenom desktop SEM, ThermoFisher Scientific, USA) at a 5 kV accelerated electron beam to maximize the contrast of graphene layers. The example of characterizing morphology and PSD using SEM is presented in Fig. 3.

For SEM observations, a few mg of each powder is sprinkled onto a conductive carbon tape and tapped to prevent the agglomeration of powder. After being exposed for 30 min to stabilize, the powder feedstock is placed on the SEM stage. The powder is observed at 1000× magnification for morphology observations, resolving scales down to 1 μm.

Observed SEM images of particles are post-processed using ImageJ software to obtain the roundness of individual particles, as shown in the top images of Fig. 3, applying the algorithm proposed by Takashimizu et al. [40]. As a result, roundness ϕ, the factor describing the smoothness of the edges of particles, is calculated as

$$\phi = C_I + (0.913 - C_{AR}) \tag{1}$$

analyzing over 500 individual particles for statistical analysis. Here, C_I is the circularity of individual particles post-processed using Image J, and C_{AR} is the factor determined by the aspect ratio of particles [40].

Along with the morphology observations, PSD analysis is performed using ImageJ software to process SEM images, as revealed on the bottom of Fig. 3. Observed SEM images are converted to binary form with Otsu's thresholding, followed by particle separation using the watershed algorithm [41]. SEM images taken at 1000× magnification are analyzed, measuring the area of individual particles by counting at least 1000 particles using the particle analysis algorithms of Image J [42]. From the measured particle areas, the diameter and the distribution of the powder are determined.

To clarify the impact of BM on morphological changes of copper and copper-graphene powder beds, μ-CT is utilized to observe the 3D-scanned images of copper, BM-copper, and BM-copper-graphene powder beds. For μ-CT scanning (Zeiss Xradia 610 Versa, Zeiss, Germany), the powder is placed in a transparent polymeric tube with a diameter of 1.5 mm, considering the target packing density of 60 %. During the loading procedures, one end of the transparent polymetric tube is sealed with instant adhesive, and powder is loaded on top of the adhesive. The entire tube containing the powder bed is then installed in the X-CT facility for observation. The sample is scanned at a tube voltage of 160 kV, power of 25 W, and a resolution of 0.7 μm. The μ-CT scanned images of each powder bed are processed for 3D reconstructions following the sequences described in Fig. 4. Detailed information of characterized powder beds such as coordination number N_c and sphericity ψ – how closely the particle shape resembles a perfect sphere – are further analyzed. The average coordination number of a powder bed is computed by dividing the total number of particle-to-particle contacts by the total number of particles. As a result, a maximum error of 3 % is experimentally obtained in the average coordination number, depending on the chosen seed radius of the particle watershed segmentation algorithm. The seed radius is selected based on the measured average radius of the particles. In addition, sphericity of the particles is calculated following [43]:

$$\psi = \frac{\pi^{\frac{1}{3}}(6V_p)^{\frac{2}{3}}}{A_p} \tag{2}$$

where, ψ represents sphericity, V_p is the volume of the particle, and A_p is the surface area of the particle. The proposed sphericity calculation method provides a maximum error less than 1 % for spherical particles [43].

3.3. Effective thermal conductivity measurements using DSC

This section describes the methods for ETC measurements using DSC to study the thermal properties of BM powder feedstocks. The extended DSC method [10,12] is employed to characterize the ETC of the powder bed by measuring the thermal resistance across the crucible using a

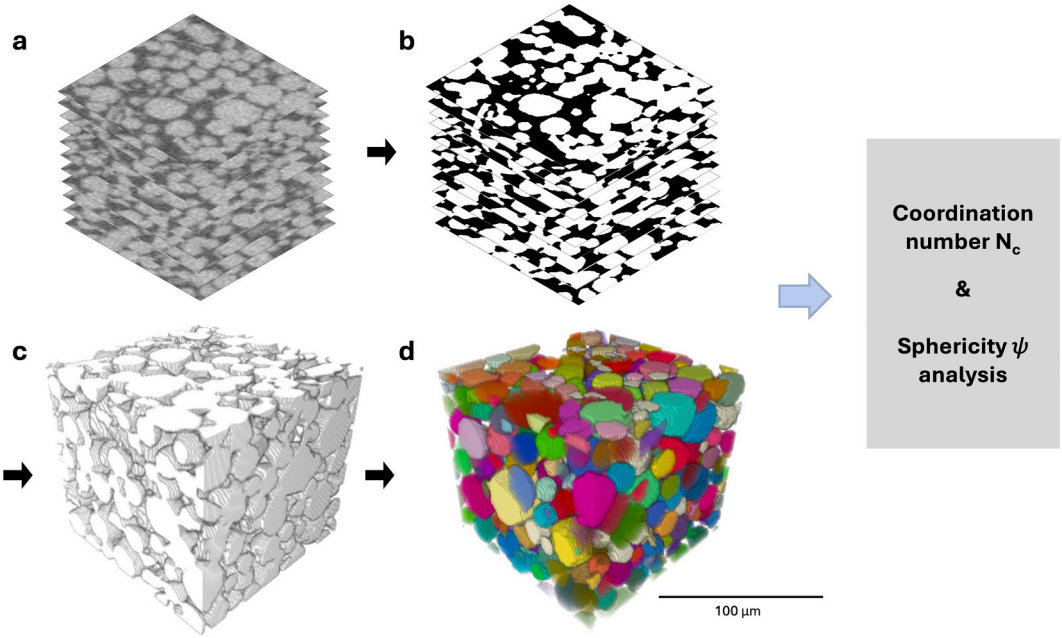

Fig. 4. Workflow for the 3D reconstruction of a powder bed scanned by μ-CT facility. The sequences follow the order from Fig. 2a to Fig. 2d. (a) 3D stacking of scanned 2D images (b) Obtaining the binary image stacks using Otsu's thresholding, (c) Merging the image stacks into a 3D reconstructed image, and (d) Coloring individual particles in the 3D image.

commercial DSC facility (DSC822e, Mettler Toledo, USA). The DSC facility records heat flow, Q, and the temperature gradient, ΔT, within a powder bed at a fixed packing density (60 % for copper and copper-graphene, considering the packing density of metallic powders for AM [44], and 30 % for graphene due to its lower packing density, resulting from the layered crystal structure of graphene. The packing density of powders is determined by the density equation (see supporting material A). An indium disc is placed on top of the powder bed as a known temperature reference, using its melting temperature T_m. Subsequently, Q and ΔT are measured while the indium disc melts (see Fig. S1 of the supporting material). The slope of the DSC scan plot ($Q/\Delta T$) is proportional to the desired ETC value and is determined under an air atmosphere at 156.6 °C (i.e. the melting temperature, T_m, of Indium). Note that the measurements are performed under ambient air atmosphere, without using any protection gas such as of Ar or N_2. This is to prevent the influence of other gases on conductivity measurements, as the thermal conductivity of the fluid phase, such as 0.0354 W/mK for air at 156.6 °C, affects the ETC of the powder bed [9]. The accompanying effects of oxidation are further discussed in Section 4.4.

Finally, the ETC value is computed as follows:

$$Q = kA\frac{(T_2 - T_1)}{L} \tag{3}$$

where, A is the cross-sectional area of the crucible containing the powder bed, L is the thickness of the powder bed, k is the ETC, and T_1 and T_2 are the temperatures at the top and the bottom of the powder bed, respectively.

The relative uncertainty of the DSC method is determined to be 3.6 % using the root mean square method [9,45] evaluating all parameters Q, A, L, and T of the DSC methodology, as shown in Table 1. The relative error of this extended DSC method for powder thermal characterizations is reported as 5–7 % [10,11]. In this case, the largest source of error comes from controlling a uniform thickness of the powder bed (L), due to difficulties in powder handling.

The reproducibility of the DSC method is evaluated by performing three repetitions of the measurements on three different powder bed samples with identical composition and packing density. The powder bed for the reproducibility test is prepared by piling up an equal mass of powder over the crucible at once, and tapping it until the crucible is completely filled with powder. Additionally, the DSC facility is calibrated based on the melting curve of a reference indium disc, until the onset of melting is reached at a temperature of 156.6 ± 0.2 °C and the enthalpy of fusion reaches 28.45 ± 1 J/g. These calibrations resolve the potential source of errors, such as convective heat loss through the Al crucible [10]. Correction of the temperature lag differences at varying heating rates is completed. This yielded a reproducibility error of approximately 5 %, as shown in Fig. S3 of the supporting material.

Lastly, the DSC-measured ETC data is compared to data obtained using other characterization methods, including transient plane source [8], laser flash analysis [45,47], and transient hot wire [9], as outlined in Table 2. This comparison aims to analyze the relative deviation of the measured ETC values by DSC compared to the other methods. In this illustration, the ETC values of SS316L powders with a PSD of 6 μm for D_{10}, 18 μm for D_{50}, and 29 μm for D_{90} are measured and compared (see Fig. S4 of the supporting material). As SS316L has limited susceptibility to oxidation [48], this way the effect of oxidation on the thermal properties at temperatures around the melting temperature of indium (~ 156.6 °C) is avoided. In addition, SS316L powder can be compared to other literature results, as it has been widely studied for ETC measurements [9,45,47]. As a result of the comparison, the measured ETC of SS316L powder using DSC is found to be 0.32 W/mK, while the result of transient plane source measurements is 0.29 W/mK, showing a ~ 9.4 % difference. This difference is readily recognized since handling of powder can cause 5 % variation in the reproducibility, while each method in addition delivers an uncertainty of ~3.6 % for DSC and ~ 2–5 % for TPS [49]. Additionally, the packing of the powder bed may vary for each method: DSC uses a 40 *mL* crucible whereas the TPS method uses a 4000 *mL* holder. This makes DSC more appropriate for controlling powder packing and characterizations, due to the smaller size of the crucible compared to the other methods. Furthermore, the relative difference in the measured ETC value of SS316L by DSC shows comparable results to those reported in other literature sources (e.g., a 9.4 % difference in the value measured by laser flash analysis of SS316L [45] in air at 156.6 °C).

In conclusion, the proposed DSC methodology for thermal characterization of powder beds is found to be as accurate as other thermal characterization methodologies and can be applied reliably to characterize universal powder beds within a general error margin of about 10 % compared to other techniques.

Table 1
Uncertainty evaluation of the extended DSC method for thermal characterizations.

Parameter	δk	k	$\delta k/k$ (%)
Q, heat flow	–	–	max 1.00 [46]
T, temperature	0.2 °C	156.6 °C	0.13
L, thickness of the sample (see Fig. S2 in supporting material)	max 0.05 mm	1.46 mm	3.42
A, cross-sectional area of a sample	0.18 mm^2	35.96 mm^2	0.50
Overall evaluated by the root mean square [9,45]	–	–	3.60

3.4. Oxidation state characterizations

In this section, we explain the method to characterize the oxidation state of the BM provided powders, specifically before and after DSC measurements. The oxidation state of the copper matrix is characterized using X-ray photoelectron spectroscopy (XPS) (PHI Quantes Physical Electronics Inc., USA) to isolate the influence of oxidation on the measured ETC. Moreover, the surface chemistry of the powders, including sp^2 hybridized carbon-carbon bonding, is examined using XPS. This is to investigate the potential oxidation of graphene during the BM process. XPS scans are performed in the range of 290 to 270 eV to detect sp^2 hybridized carbon-carbon bonding in graphene. Additionally, XPS scans in the range of 975 to 923 eV are conducted to detect oxidation states on the surface of the copper matrix [50].

4. Results & discussion

In this section, we examine the impact of BM on the microstructural and thermal properties of copper, graphene and copper-graphene composite powders. To achieve this, the influence of BM duration time on copper (Section 4.1), the impact of BM time on graphene powders (Section 4.2), and, lastly, the effect of varying graphene wt% on copper-graphene composite powders (Section 4.3) is discussed to gain a quantitative understanding of each preparation stage for copper-graphene powders. In Section 4.4, the effect of BM and DSC measurements on the composition of graphene and the oxidation state of copper is explored.

4.1. Effect of ball milling on copper powders

BM can significantly alter the morphology and PSD of copper powders as milling time increases, due to the impact energy and shear forces applied to powders during the BM [51,52]. These morphology and PSD changes may influence the thermal properties of the resulting powder beds.

In this section, we examine the effect of BM time on copper powders' microstructural and thermal properties, varying BM times from 6 h to 12 h and 24 h. This analysis yields optimal BM time for producing

Table 2
Effective thermal conductivity data of SS316L characterized by several methods.

Materials	Characterization technique	Packing density (%)	Temperature (K)	Atmosphere	Effective thermal conductivity(W/mK)	References
SS316L powder	DSC (our measurement)	60	429.6	Air	0.32	–
	Transient plane source (our measurement)	60	429.6	Air	0.29	–
	Laser flash analysis	unknown	429.6	Air	0.35	[45]
	Laser flash analysis	52.3	423	He	0.19	[47]
	Transient hot wire	54	429.6	Ar	0.27	[9]

copper, graphene and copper-graphene powders in terms of their microstructural changes and resulting thermal properties.

As shown in Fig. 5, the morphology of copper powder changes from the initial spherical shape with spheres of average diameter 22 μm, to a polyhedral shape after 6 h of BM, further shifting to a flat flake shape after 12 h and 24 h of BM. The BM process induces several qualitatively different mechanical deformation phases [53]. BM is known to first induce a plastic deformation, followed by the flattening of the particles by prolonged exposure to shear forces. In addition, further transition results in cold welding and fracturing phases until a dynamic balance is reached, often exposing a rich diversity of shapes. The BM copper powder also exhibits such a transition from spherical to polyhedral at 6 h BM resulting from the initial plastic deformation. Flakes are seen to form after 12 h - 24 h from shearing-induced particle stretching. Prolonged BM results in significant qualitative changes in the particle morphology, which not all yield powders suitable for AM based on L-PBF.

Detailed microstructural changes in copper powders are displayed in Fig. 6, highlighting PSD changes during extended BM times. As shown in Fig. 6a-b, the PSD slightly changes, displaying a 15 % change in the D_{50} value from 22 μm to 19 μm after 6 h of BM. This shift in PSD indicates initial fracturing of the larger particles, likely caused by high-energy collisions [52]. The PSDs of the initial copper and 6 h BM copper powders present D_{10} – D_{50} – D_{90} values of 13 μm – 22 μm – 32 μm and 6 μm – 19 μm – 28 μm, respectively. This shift presents the surface fracturing in copper powder during the first 6 h of BM [54]. Fig. 6c further shows PSD changes after 12 h and 24 h of BM, indicating the morphology change to a flake-like shape. The D_{50} values after 12 h and 24 h BM reach 38 μm and 56 μm, respectively. Additionally, 12 h and 24 h BM copper shows an average thickness of 4.94 ± 0.13 μm for 12 h BM copper and 1.94 ± 0.03 μm for 24 h BM copper, based on the SEM statistical analysis, presented in Fig. S5 of the supporting material.

Hence, the PSD analysis and thickness measurements indicate particles stretching in flaky powders, with an increased D_{50}, but reduced thickness after prolonged BM time. Hence, the use of the D_{50} values for the characterization of copper powders with a relatively large difference in morphology needs to be considered with care. While this provides a clear interpretation of the PSD changes for largely spherical particles, it may be confusing in the case of flakes.

Modified morphology and size of BM copper powders exhibit an immense influence on structural and thermal properties, such as the relative connection of particles, indicated by their contact radius, and ETC value [35]. It is known that the contact radius and ETC value are mutually interactive, resulting in a higher ETC when powder particles have better connectivity due to an increased contact radius.

To elucidate the impact of morphological and dimensional changes on these properties, first, the effect of BM time on the thermal properties is analyzed, as shown in Fig. 7a, along with packing density variations. The thermal properties of copper powders change notably with BM time, with ETC decreasing from 0.43 W/mK for pristine pure copper to 0.39 W/mK after 6 h BM, 0.33 W/mK after 12 h BM, and finally 0.24 W/mK after 24 h BM. A strong decrease in packing density is also observed from 60 % for pristine and 6 h BM copper to 40 % for 12 h BM copper and further decreasing to 30 % for 24 h BM copper. Note that this decrease in ETC is not only related to the reduction in packing density, but also impacted by morphology transformation of the powders.

Maxwell-Garnett's classical estimation of ETC of powder beds (k_{ETC}) is a basic formulation with incorporated effects of packing density (f_s), geometrical factor (β), and conductivities of fluid (k_f) and solid (k_s) phases [55,56]. As the Maxwell-Garnett model considers the scenario in which individual particles do not touch each other, it represents a lower bound for ETCs in realistic settings. The classical Maxwell-Garnett model for non-interacting particles is formulated as:

$$k_{ETC} = \frac{(1 - f_s) \bullet k_f + f_s \bullet \beta \bullet k_s}{(1 - f_s + f_s \bullet \beta)} \quad (4)$$

where, β is expressed as:

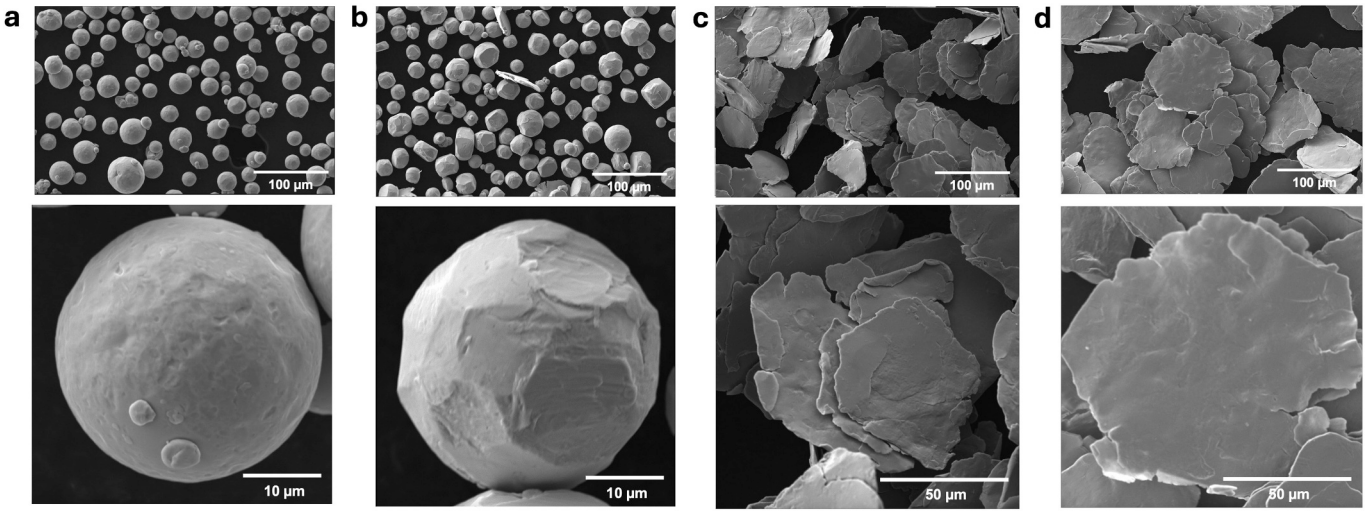

Fig. 5. SEM images of copper powders after different durations of dry ball milling. (a) As-received copper powder, copper powders after (b) 6 h, (c) 12 h, and (d) 24 h ball milling, respectively. The bottom-sided images present magnified views of individual copper particles.

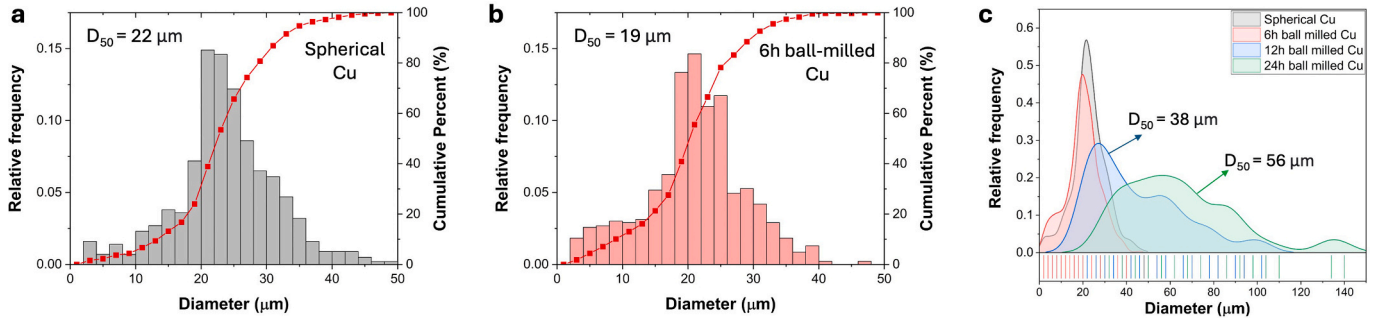

Fig. 6. Particle size distribution (PSD) characterization of copper powders before and after ball milling (BM). (a-c) PSD of (a) pristine spherical copper, (b) copper after 6 h of BM, and (c) all copper powders combined after various BM times.

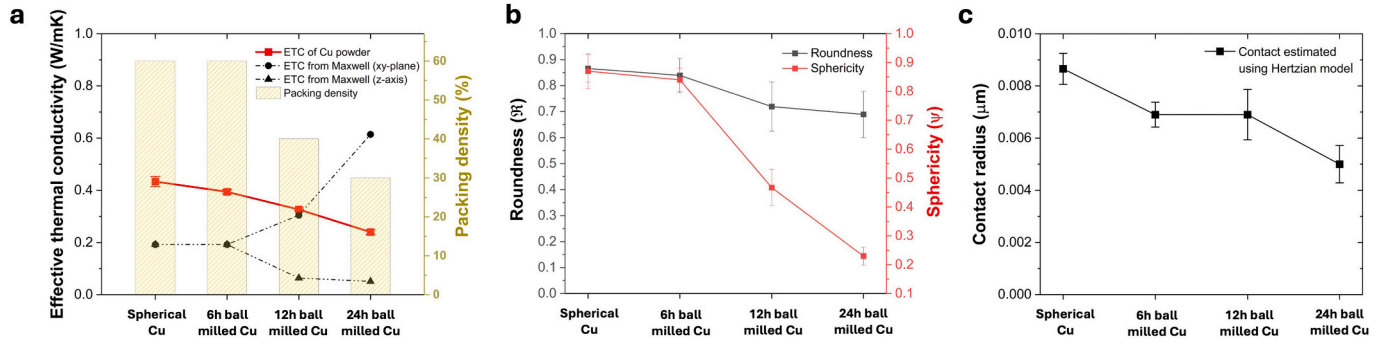

Fig. 7. Influence of ball milling (BM) on copper powders (a) Effective thermal conductivity (ETC) of BM copper powders. The ETC of copper powders is compared with predicted values from Maxwell-Garnett's model. (b) Morphological change including roundness and sphericity, (c) Contact radius variation estimated by Hertzian model for BM coppers.

$$\beta = \frac{1}{3}\sum_{j=1}^{3}\frac{k_f}{k_f + L_j\left(k_s - k_f\right)} \tag{5}$$

The β value is obtained by averaging the depolarization factor L for particles along the x, y, and z coordinates. The depolarization factor L in x, y, and z directions corresponds to L_1, L_2, and L_3. Hence, $L_1 = L_2 = L_3 = \frac{1}{3}$ for a spherical particle, whereas L for a flake-like particle is computed as:

$$L_1 = L_2 = \frac{\mathrm{AR}\left(\frac{\pi}{2} - ArcSin(AR) - AR\sqrt{1-AR^2}\right)}{2\left(1-AR^2\right)^{3/2}} \tag{6}$$

$$L_3 = 1 - L_1 - L_2 \tag{7}$$

Here, AR indicates the aspect ratio of the flaky particle, particularly the ratio of thickness to diameter [56]. In our case, the aspect ratio of the flaky particles is determined to be 0.13 for 12 h BM and 0.035 for 24 h BM, using the average D_{50} and particle thickness measured in Fig. 6c and Fig. S5, respectively. Accordingly, Maxwell-Garnett's model for flaky particles predicts the individual ETCs for particles that are vertically aligned (based on L_1 and L_2), and horizontally aligned (based on L_3). Note that the realistic ETC for flaky particle is expected to fall between two values, depending on the individual influence of each orientation.

In Fig. 7a the Maxwell-Garnett prediction is compared to the measured values, showing the additional effect of pristine and 6 h BM copper, due to particle-to-particle interactions. For flaky particles, the Maxwell-Garnett prediction presents two cases. In the first case, heat is assumed to flow predominantly through a flat and large surface (xy-plane), while in the second case, it flows through the thin thickness direction (z-plane). The measured ETCs for the flaky particles fall within the range between the upper and lower model predictions as BM time increases, implying the reduced influence of particle-to-particle contact.

To reveal the comparative influence of particle interactions, the particle contact radius is evaluated using the classical contact mechanistic model of Hertzian [57]. The Hertzian model describes how elastic spherical bodies interact under external forces, based on the material's mechanical properties. As an external force is not applied during the ETC measurement, only the influence of gravitational forces is considered. Accordingly, the contact radius a is determined as:

$$a = \sqrt[3]{\frac{3FR^*(1-\nu^2)}{4E}} \tag{8}$$

where, F is the contact force, R^* is the effective radius, ν is the Poisson's ratio, and E is the elastic modulus.

In a powder bed with a certain porosity, the contact force F is defined as:

$$F = \frac{4\pi {R_{loc}}^2 P}{N_c f_s} \tag{9}$$

where, R_{loc} is local radius of curvature near the contact point, P is the overburden gravitational pressure, and N_c is average coordination number [58].

R_{loc} is determined by the particles' average size, roundness and sphericity based on:

$$R_{loc} = R_{\mathrm{avg}} \bullet \phi \bullet \psi \tag{10}$$

where, R_{avg}, ϕ, ψ are the average radius, roundness, and sphericity of particles, respectively.

To estimate the R_{loc} for BM coppers, the roundness and sphericity of the particles are investigated as shown in Fig. 7b, following the methodologies described in Section 3.2. The results reveal that the initial 6 h of BM slightly decreases the roundness and sphericity from approximately 0.87 for spherical copper to 0.84 for 6 h BM copper. However, the sphericity of particles significantly decreased to 0.46 at 12 h and

0.23 at 24 h BM, due to the morphological transition to flaky particles.

Using the obtained R_{loc}, and the input summarized in Table 3, the estimated particle contact radius for BM copper is displayed in Fig. 7c. As the influence of BM increases, the average contact radius decreases from 0.0087 ± 0.0009 μm for spherical copper to 0.0069 ± 0.0007 μm for 6 h BM, 0.0069 ± 0.0015 μm for 12 BM copper, and 0.0051 ± 0.0011 μm for 24 h BM copper.

In other words, BM of copper leads to a reduction in the powder particles' contact radius, supporting the diminished influence of particle interactions on ETCs observed in Fig. 7a. Collectively, BM copper undergoes a drastic morphological transition from spherical to flaky shape, leading to reduced particle-to-particle interactions and therefore enhanced influence of heat conduction through the fluid phase.

The morphological change to flaky powder and resulting lower ETC by BM renders the copper powder less suitable for AM. This suggests that BM times should be restricted to 6 h or less for copper powders, to maintain a near-spherical shape for the individual powder particles. The relevance of microstructural features of particles on the ETC will be further discussed in Sections 4.2. and 4.3 considering graphene and copper-graphene mixtures.

4.2. Effect of ball milling on thermal conductivity of graphene

BM time was shown to affect the thermal and microstructural properties of copper powders. In this section, the impact of BM on graphene powders by changing the BM time from 6 h to 12 h and 24 h is examined. Fig. 8a-d shows the process of graphene powder production from bulk graphite flakes. As a result of BM, the graphite flakes undergo significant microstructural changes as BM time increases, displaying the accumulated results of impact and shear forces in graphene and graphite. Eventually, this leads to the exfoliation of graphene sheets, by disconnecting the interlayer Van Der Waals bonding [30].

During the BM of graphite flakes to yield graphene powder, the transition from graphite to graphene proceeds gradually with BM time, as is observed from the SEM images. This is also supported by the change in the graphene's aspect ratio – the ratio of thickness to lateral size – as shown in the Fig. S6a of the supporting material. At a fixed packing density of 30 % for all graphene/graphite powders, the ETC continuously decreases as BM time increases. The microstructural changes considerably alter the thermal properties of powders as shown in Fig. 8e. As thermal characterization of graphene (or graphite) powders is performed at a fixed packing density of 30 % for all powders, the observed changes are not due to the embedded air. The BM of graphene decreases the ETC from 0.35 W/mK for graphite powder to 0.29 W/mK after 6 h BM, 0.19 W/mK after 12 h, and finally to 0.10 W/mK after 24 h. Hence, after 24 h of BM, the ETC is reduced by about 70 % compared to the original graphite powder.

Again, the Maxwell-Garnett model for flaky powders provides a good estimation of the ETC, as the graphene (or graphite) powder packing density (30 vol%) is low enough to exclude particle-to-particle interactions [61]. For the model prediction, thermal conductivity of graphene is set to three values: 1000 W/mK, 2000 W/mK, and 3000 W/mK, adopted from other literatures [62,63]. Interestingly, the measured ETC values fall within the range of predicted ETC values for vertically aligned (*xy*-plane) and horizontally aligned (*z*-plane) cases of the Maxwell-Garnett model, displaying a similar decreasing trend. This implicates that the BM graphene (or graphite) flakes are randomly distributed, not aligned in a specific plane. The decreasing trend of ETC originates from the increasing aspect ratio *AR*, particularly the thickness-to-lateral size of graphene, as BM time increases. According to the Maxwell-Garnett model, the intrinsic thermal conductivity of graphene does not influence the predicted ETC values at all between 1000 W/mK, 2000 W/mK and 3000 W/mK. Therefore, the ETC of graphene (or graphite) powder is primarily modified by the aspect ratio of the graphene particles.

The graphene powder discussed in this section will be used to prepare copper-graphene composite powders in Section 4.3. To ensure AM printability, it is important to use thin graphene sheets for obtaining a uniform coating. In addition, a high intrinsic thermal conductivity is necessary for heat transfer applications. An increased BM time facilitates graphene thinning, ensuring a uniform coating of graphene on copper powders. However, extending BM time also reduces the intrinsic thermal conductivity of graphene, as revealed by Raman spectroscopy characterizations (see Fig. S6b of the supporting material). This reduction in thermal conductivity is attributed to increased internal defect densities by BM, which intensify phonon scattering [64]. Overall, a complementary BM time of 12 h is chosen, balancing these two factors.

4.3. The effect of graphene addition on copper powders

In this section, the effect of graphene powder addition on copper powder is investigated. To produce copper-graphene composite powders, BM is used to mix copper and graphene powders. Pristine spherical copper is used as the matrix material, while 12 h BM graphene powder serves as the additive. To ensure uniform mixing, 6 h of BM time is applied to minimize morphological changes to the copper particles, based on the observations discussed in Section 4.1. The production process is illustrated in Fig. 9. After mixing of copper with different wt% of graphene, the change in microstructure is observed and the consequences for the thermal properties are quantified.

To understand the impact of graphene addition on the microstructure, SEM imaging and PSD analysis are first performed. 6 h BM of the copper-graphene composite powder is investigated and the wt% of the graphene addition is varied from 1 wt% to 3 wt%, 10 wt% and 20 wt%. To isolate the impact of graphene addition, 6 h-BM copper without graphene additive is analyzed for comparison.

As shown in Fig. 10a-e, the graphene phase coats the surface of copper particles in a patchy way, which depends qualitatively on the graphene wt%. Notably, graphene not only covers the copper particles, but the excess graphene also forms a separate graphene powder, homogeneously mixed with the graphene-coated copper. The overall PSD of copper particles is altered by the powder formed by the excess graphene particles. The PSD change of copper powder is first observed after 6 h of BM. After 6 h of BM, the pure copper powder has D_{10} – D_{50} – D_{90} values of 6 μm – 19 μm – 29 μm, while adding 1 wt% graphene induces a shift to 2 μm – 18 μm – 31 μm. In this case, the PSD exhibits a bi-modal distribution, see Fig. 10g, due to the smaller graphene and relatively large copper particles.

At 3 wt% graphene, a PSD of 2 μm – 10 μm – 28 μm is obtained, further reducing to 2 μm – 6 μm – 22 μm for 10 wt% graphene, and down to 2 μm – 6 μm – 14 μm for 20 wt% graphene. The distribution generally shifts to a single peak at the left edge of the graph, due to the high count of single graphene particles compared to graphene-copper composite particles. Thus, adding graphene to the copper particles generally reduces the overall D_{10} – D_{50} – D_{90} values associated with the PSD and also

Table 3
Particle contact area calculation for ball-milled copper using Hertzian theory [57].

Particle type	Poisson's ratio ν	Young's modulus E	R_{loc} (μm)	Overburden pressure P (Pa)	Coordination number N_c	Force F (nN)	R* (μm)
Spherical Cu	0.34 [59]	110 GPa [60]	8.29	104.4	5.8	25.9	4.14
6 h ball-milled Cu			6.70	104.4	5.7	17.2	3.35
12 h ball-milled Cu			6.38	78.9	6.0	16.8	3.19
24 h ball-milled Cu			4.42	66.2	6.0	9.0	2.21

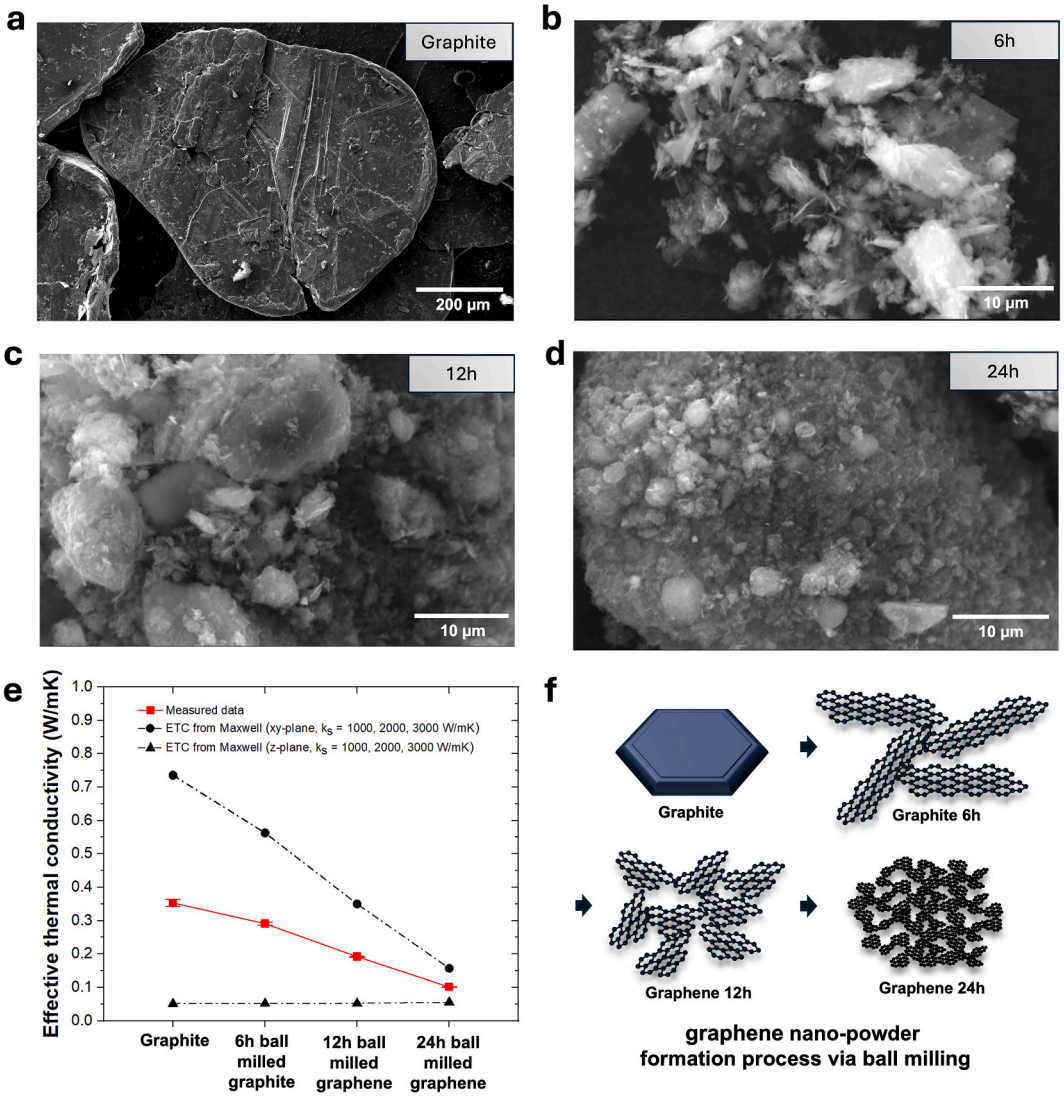

Fig. 8. Characterizations of graphene powders after ball milling. SEM images of (a) graphite, (b-d) graphene after (b) 6 h, (b) 12 h, and (c) 24 h ball milling, respectively. (e) The effective thermal conductivity of all graphene powders based on their ball milling time. The dotted line represents the ETC predictions provided by Maxwell's model; note that the modelled thermal conductivity of graphene, k_s, is irrelevant (f) Schematic images of the graphene ball milling process.

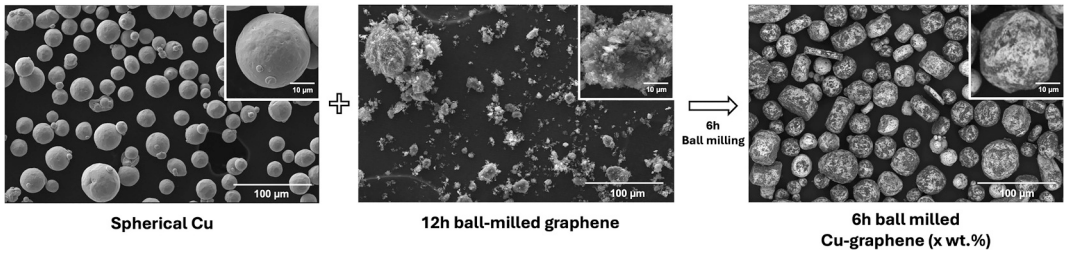

Fig. 9. Production process of copper-graphene composite powders with different wt% of graphene. Spherical copper and 12 h ball-milled graphene are mixed through 6 h of ball milling.

displays the presence of excess graphene particles that do not adhere to the copper particle surfaces.

As shown in Fig. 10, adding graphene to copper particles induces multiple microstructural transitions in the composite powders, including the morphological shift to a polyhederal-shape and the reduction in overall PSD. Such microstructural changes lead to alterations in AM suitability, due to the modifications in powder flowability and ETC value. A smaller PSD results in increased particle cohesive forces and decreased flowability [65]. Thus, based on the PSD study, adding higher graphene wt% to the copper particles adversely affects the flowability of the powders, making them less suitable for powder bed-based AM processing.

Since the aim of the BM process is to produce graphene-coated copper particles, the presence of additional excess graphene powder requires further study to improve the attachability of graphene when such composite powders are used as feedstock for AM. Along with the

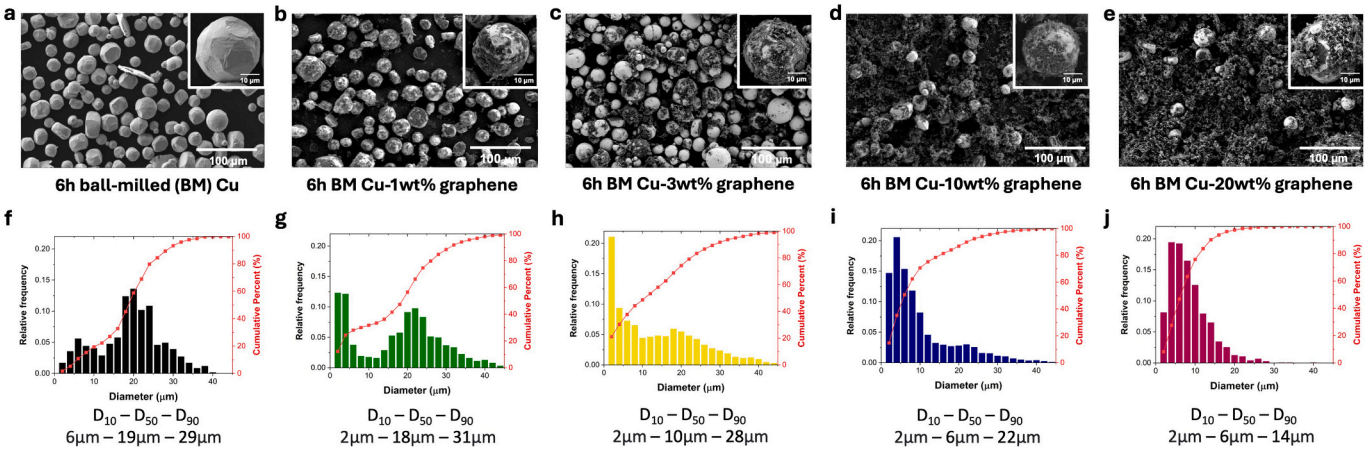

Fig. 10. Microstructural characterizations of copper-graphene composite powders with different wt% of graphene addition. SEM images of 6 h (a) ball-milled copper (b) ball-milled copper with 1 wt% graphene, (c) ball-milled copper with 3 wt% graphene, (d) ball-milled copper with 10 wt% graphene, and (e) ball-milled copper with 20 wt% graphene. Inset images display the morphology of a single composite particle showing graphene coating of the copper spheres against a growing background of graphene. Particle size distribution of 6 h (f) ball-milled Cu, (g) ball-milled Cu with 1 wt% graphene, (h) ball-milled copper with 3 wt% graphene, (i) ball-milled copper with 10 wt% graphene, and (j) ball-milled copper with 20 wt% graphene.

influence of the reduced PSD on AM suitability, the ETC of powder bed is examined to evaluate the overall AM suitability of copper-graphene powders, following the heat conduction regimes illustrated in Fig. 11.

Based on the microstructure observations, the produced copper-graphene powders can be categorized into two heat conduction regimes, depending on the dominant particle (see Fig. 11). Regime 1 primarily considers heat conduction through copper-to-copper particles. In this regime, copper with a low wt% of graphene, (e.g., 1 wt%) is considered comparable to copper-to-copper particles. Regime 2 however is dominated by copper-to-graphene conduction and vice versa, due to the excess graphene powder. Copper that is BM with high graphene wt % (e.g., 3 wt%, 10 wt% and 20 wt%) falls into this category. Copper-1 wt % graphene is considered at the border between both regimes and serves as a threshold point before having excess graphene in the powder feedstock.

To analyze the heat conduction mechanisms in copper-graphene composite powders, two different thermal models are applied. For Regime 1, the thermal model of a resistance network for spherical particles is used, in comparison to the Maxwell-Garnett model [66]. For Regime 2, the extended Maxwell-Garnett model for effective medium consisting of a three-phases system (Cu, graphene, and air) is used. In Regime 1, the thermal resistance between individual particles forms a network, which can be used to predict the particle-to-particle solid conduction contribution to the powder bed's ETCs. In Regime 2, the extended Maxwell-Garnett model allows for the consideration of the individual contributions of graphene-coated copper particles and excess graphene to the overall ETC.

To investigate the heat conduction for Regime 1, microstructural transition from spherical to slightly polyhedral copper particles during the BM is observed using X-ray μ-CT scans. Scans are conducted for copper powders and for the copper-1 wt% graphene reference mixture, after 6 h of BM. As shown in Fig. 12a-f, the morphology changes of the spherical copper powder bed during 6 h BM are evident, displaying a transition from spherical to polyhedral shapes. This trend is also observed for the BM copper-1 wt% graphene powder bed. For the 6 h BM copper-1 wt% graphene powder bed, the morphology of the larger particles exhibits a similar polyhedral shape, while the smaller particles appear fragmented graphene flakes. The packing densities of the measured powder bed are approximately 60 %, 63 %, and 60 % for spherical copper, 6 h-BM copper, and 6 h-BM copper-1 wt% graphene powder beds, respectively. Here, the average coordination number of neighboring particles (see Fi. 12 g-i) and the average sphericity of the particles (see Fig. 12j-l) are determined for spherical copper, BM copper, and BM copper-1 wt% graphene powder beds using 3D-reconstructed images. The coordination numbers are quite similar for the individual powder beds, exhibiting 5.8 ± 0.1 for spherical copper, 5.7 ± 0.1 for BM copper, and 6.2 ± 0.2 for BM copper-1 wt% graphene. BM copper-1 wt% graphene exhibits a slightly higher coordination number, likely due to the presence of small graphene flakes trapped between the copper particles. Additionally, the sphericity of the particles decreases from 0.87 ± 0.06 to 0.84 ± 0.04 after BM and further down to 0.82 ± 0.09 after the addition of graphene powders. This decreasing trend is associated with the morphology transition from spherical to polyhedral shapes, and the additional incorporation of graphene flakes. Since all powder beds exhibit high levels of sphericity, the ETC of pristine copper, BM copper, and BM copper-1 wt% graphene can be predicted following the approach of Gusarov and Kovalev [66]. This gives a prediction for solid contact conductivity of granular particles, considering them as a thermal resistance network. This model provides the insight into how continuity in the solid phase contribute to the ETC of powder bed, considering the contact conduction between particles.

$$K_{solid-contact} = K_{particle} \frac{f_s \bullet N}{\pi} \bullet \frac{a}{D} \tag{11}$$

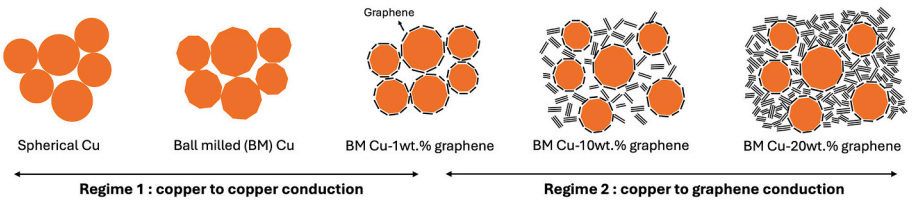

Fig. 11. Heat conduction regimes in BM copper and BM copper-graphene powders. Heat conduction in spherical copper, BM copper, and BM copper with 1 wt% can be compared within regime 1, while BM copper-1 wt%, 10 wt%, and 20 wt% can be compared within regime 2.

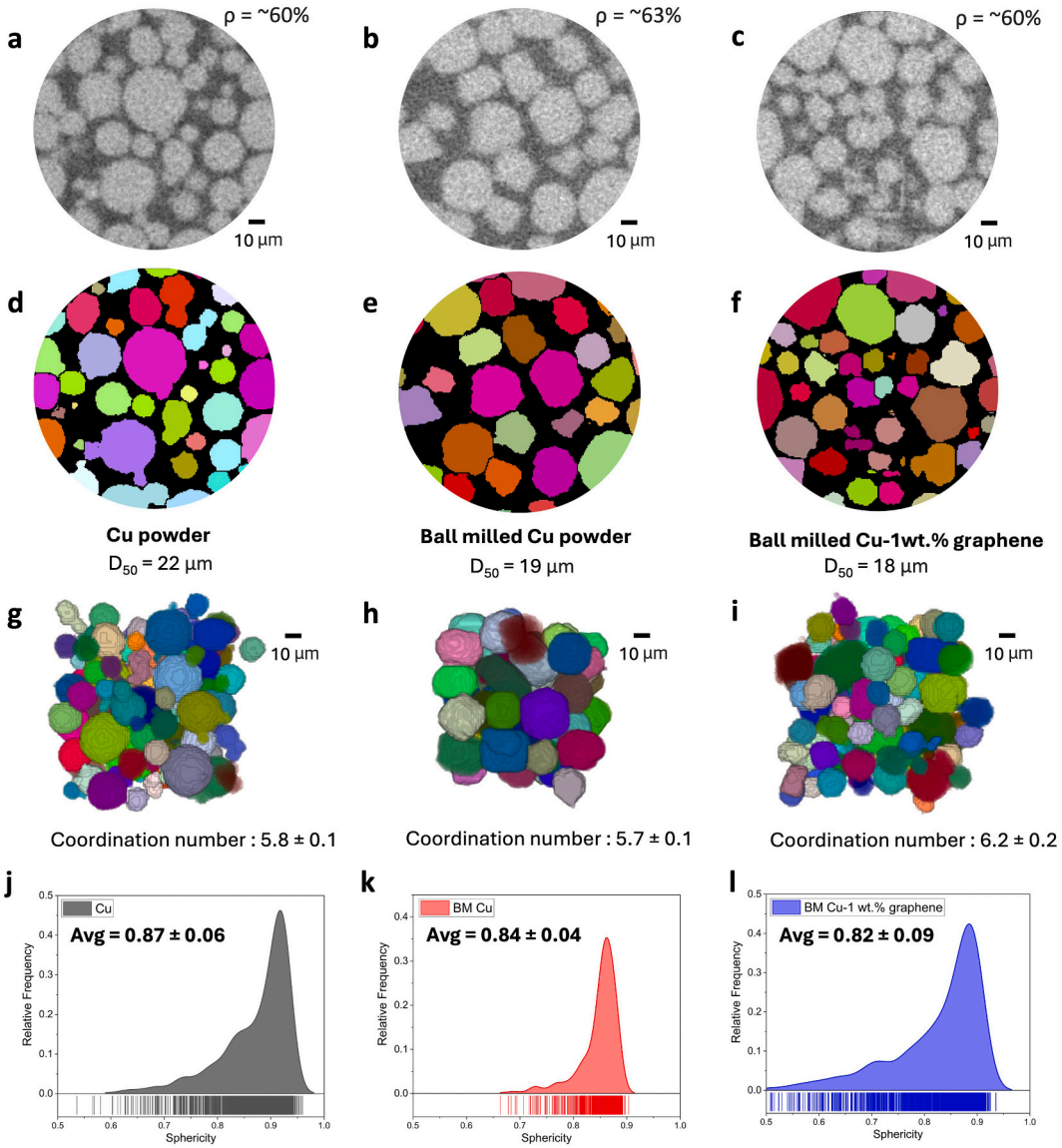

Fig. 12. CT scanning characterization of spherical copper, 6 h ball-milled copper, and ball-milled copper-1 wt% graphene composite powder beds (a-c) CT-scanned 2D images of (a) spherical copper powder bed, (b) 6 h ball-milled copper powder bed, and (c) 6 h ball-milled copper-1 wt% graphene powder bed. (d-f) Corresponding colored images to identify individual particles of (d) spherical copper powder bed, (e) 6 h ball-milled copper powder bed, and (f) 6 h ball-milled copper-1 wt % graphene powder bed. (g-i) 3D reconstructed powder beds of (g) spherical copper, (h) 6 h ball-milled copper, and (i) 6 h ball-milled copper-1 wt% graphene. (j-l) Sphericity analysis of (j) spherical copper, (k) 6 h ball-milled copper, and (l) 6 h ball-milled copper-1 wt% graphene powders.

where, $K_{particle}$ [W/mK] is the intrinsic thermal conductivity of the particle, f_s is the volume fraction of particles (here 0.60 or 0.63), N is the coordination number, a [μm] is the radius of the contact area, and D [μm] is the average particle diameter.

Accordingly, the ETC of powder beds can be obtained as a function of the contact area, provided the thermal conductivity of a graphene-coated single particle $K_{particle}$ is determined first.

The graphene-coated copper particles can be considered as core-shell particles, with copper as the core and graphene as the shell (see Fig. 13a). The thermal conductivity of the core-shell copper-graphene particles can be approximated using the internal Maxwell-Garnett approximation [67]. In this case, the thermal conductivity of the core-shell particle is approximated using a weighted average of the conductivities based on the volume fraction [67]. Following this approach, for spherical core-shell particles, the ETC can be predicted as:

$$K_{core-shell} = K_{shell} \bullet \frac{K_{core} + 2K_{shell} + 2(K_{core} - K_{shell})f_{core}}{K_{core} + 2K_{shell} - (K_{core} - K_{shell})f_{core}} \quad (12)$$

where, the thermal conductivity of the shell phase is denoted by K_{shell}, that of the core phase by K_{core}, and the volume fraction of the core phase by f_{core}. In this case, K_{core} is set to 390 W/mK for the core copper phase, and K_{shell} is set to 2000 W/mK for graphene shell. The latter being the middle value within the typical range of intrinsic thermal conductivity for graphene, as discussed in Section 4.2. When 1 wt% (3.84 vol%) of graphene is added to the copper powder, the f_{core} value corresponds to 0.9616 based on the volume fraction of the copper matrix. As a result, $K_{core-shell}$ is expected to be 435.7 W/mK. The $K_{core-shell}$ values obtained from Eq. (12) are used to substitute $K_{particle}$ in Eq. (11) to represent BM copper-1 wt% graphene particles.

Hence, $K_{solid\text{-}contact}$ for spherical copper, BM copper, and BM copper-1 wt% graphene powder beds is determined using Eq. (11), using the obtained parameters including, $K_{particle}$, f_s, N, D, and a. The contact radius a estimated in Fig. 7c is employed for spherical copper and BM copper, while the contact radius for copper-1 wt% graphene is additionally approximated using the inputs summarized in Table 4, following Hertzian theory [57].

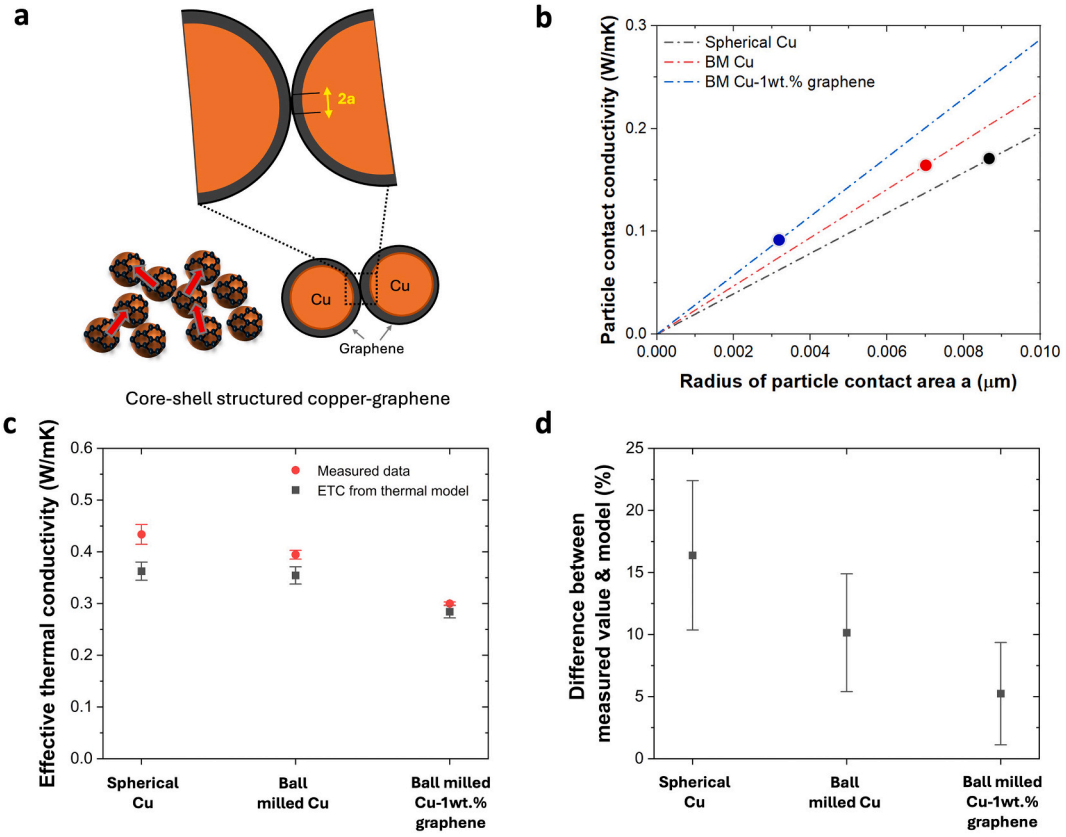

Fig. 13. Effective thermal conductivity predictions of spherical copper, ball-milled copper, and copper-1 wt% graphene composites. (a) Schematic illustration of copper-1 wt% graphene composite particles (core-shell structure) based on SEM observations. (b) Particle contact conductivity predicted by thermal resistance network model. The colored dotted lines represent the model predictions, and the three icons denote the obtained conductivity value from contact radius *a*. (c) Comparison of effective thermal conductivity between measured data and the predicted values, and (d) Analysis of their difference.

Table 4
Particle contact area calculation for ball-milled copper-1 wt% graphene.

Particle type	Roundness	Sphericity	Poisson's ratio	Young's modulus	R_{loc} (μm)	Overburden pressure P (Pa)	Coordination number N_c	Force F (nN)	R^* (μm)	Contact radius a
BM copper-1 wt% graphene	0.85 ± 0.06	0.82 ± 0.09	0.19 [68]	1 TPa [16]	6.27	0.27	6.2	13.9	3.14	0.0032 ± 0.0004

Accordingly, the equivalent particle contact conductivity associated to solid contact conduction for spherical copper, BM copper, and BM copper-1 wt% graphene are predicted as a function of the radius of the contact area using the thermal resistance network model, as depicted in Fig. 13b.

As a result, the predicted particle contact conductivity values are represented by the three larger icons, showing 0.17 W/mK for spherical copper, 0.16 W/mK for BM copper, and 0.09 W/mK for BM copper-1 wt % graphene. The predicted particle contact conductivity value slightly drops after BM and significantly decreases with the addition of 1 wt% of graphene, due to the diminished particle contact radius. The reduction due to graphene addition is mainly caused by the mechanical properties of graphene, such as Poisson's ratio and Young's modulus, while other parameters remain similar. Note that the estimated particle contact conductivity by the thermal resistance model represent the contribution of particle-to-particle solid contact conduction. In contrast, the conductivity predictions using the Maxwell-Garnett model consider solid-fluid-solid conduction, as particle-to-particle interactions are minimal.

The predicted ETC value for powder bed includes the two cases: solid-to-solid conduction and solid-fluid-solid conduction, enabling the estimation of the overall ETCs by combining the two individual contributions. The ETC predicted by the two combined contribution is displayed in Fig. 13c, alongside the experimentally measured data. Based on the thermal model and measured values, the ETCs are 0.36 W/mK and 0.43 W/mK for spherical copper, 0.35 W/mK and 0.39 W/mK for BM copper, and 0.28 W/mK and 0.30 W/mK for BM copper-1 wt% graphene, respectively. Fig. 13d shows the differences between model predictions and measured values. As shown in Fig. 13c, the values predicted by thermal model slightly underestimate the ETC compared to the measured values. This discrepancy could originate from differences between the averaged input parameters and the actual values (e.g., using the D_{50} value for particle size). However, more importantly the trend related to BM and graphene addition is captured by the model.

In summary, the particle contact contribution is minimal after the addition of graphene, and the combined effects of particle contact conduction and solid-fluid-solid conduction provides a better prediction compared to measured ETCs.

In Regime 2, the characterized particle conductivity for the core-shell copper-graphene particles is used to quantify heat conduction through the complex powder consisting of core-shell particles with 3 wt %, 10 wt% and 20 wt% addition of graphene. Heat conduction through this complex system is analyzed using the extended Maxwell-Garnett approximation for multi-component systems, by mainly considering solid-fluid-solid heat conduction [56]. Here, particle-to-particle contact

conduction is excluded, as the addition of graphene minimizes the particle contact radius, revealed by the Regime 1 analysis. In this approach, the composite powder is treated as a system with an effective medium consisting of homogenized core-shell particles and air, with excess graphene filler, as illustrated in Fig. 14a. The overall ETC of composite powder is then obtained through

$$k_{ETC} = \frac{(1 - f_s) \bullet k_f + \sum f_j \bullet \beta_j \bullet k_j}{\left(1 - f_s + \sum f_j \bullet \beta_j\right)} \tag{13}$$

as an extension of Eq. (4), where j corresponds to individual solid phase particle.

As a result, the ETC values predicted by the extended Maxwell-Garnett and experimentally measured values are presented in Fig. 14b. The measured values, i.e. 0.287 W/mK for 3 wt% graphene, 0.27 W/mK for 10 wt% graphene, and 0.26 W/mK for 20 wt% graphene, slightly decreases as the graphene content increases. In addition, the measured values fall within the range between the upper and lower predictions, where the graphene particle is vertically aligned (xy-plane) and horizontally aligned (z-plane). The measured values are most close to the estimation for the horizontal case (z-plane). Thus, it is likely that graphene is more horizontally aligned when mixed with the core-shell copper-graphene particles, possibly due to better separation of the agglomerated graphene via mixing. As revealed by the thermal model, the contribution of particle-to-particle contact conduction is limited compared to particle-fluid-particle conduction, as expected.

In essence, heat conduction in copper-graphene composite powder can be divided into two cases. One in which the added graphene powder is entirely used for coating the copper particles. The other in which excess graphene powder exists between the core-shell structured, graphene-coated copper particles. In the first case, the addition of graphene decreases the ETC of the powder bed, as the coated graphene reduces the contact radius, resulting in less effective heat conduction. In the second case, the solid-fluid-solid heat conduction is dominant over the contact-induced conduction, and continuously influenced by the reduced contact radius between graphene particles.

Overall, it is evident that adding graphene does not inherently increase the overall ETC of the composite powder. Instead, the thermal properties of the composite powder are influenced by multiple factors, such as microstructural characteristics and interactions between the individual particles.

Building upon the investigation of BM copper-graphene powders for AM suitability, lower flowability and reduced ETC for higher contents of graphene makes the composite powder less applicable for AM. However, selecting the proper amount of graphene requires a balanced approach, also considering the expected increase in thermal conductivity by graphene addition of the fabricated (end-)parts.

4.4. Oxidation effects on the thermal conductivity of powders

In this section, the influence of oxidation on the thermal properties of copper and copper-graphene composite powders is characterized. As discussed in the previous section, BM decreases the ETC of both copper and graphene powders, and the addition of graphene further reduces the ETC of the copper-graphene composite powders. However, the effect of oxidation on the ETCs is not well established, despite its potential detrimental impact on thermal properties. Therefore, the ETC variation during the DSC runs of both pristine spherical copper and BM copper-1 wt% graphene powder is selectively characterized. This is also done to distinguish the effect of BM on the ETC from oxidation, as oxidation typically lowers thermal conductivity. Hence, the oxidation state of pristine copper and copper-1 wt% graphene before and after eight DSC runs is analyzed using XPS. In addition, the microstructure of the powders is observed using SEM. Before analyzing the oxidation states, the carbon-carbon bonding in the graphene layer of the copper-graphene powder is characterized to confirm the sp^2 hybridization bonding before and after the DSC runs (see Fig. 15a). This is to confirm whether the graphene is still intact after multiple DSC runs. As shown, the DSC runs do not destroy the chemical bonding of the graphene. Graphene bonding remains intact as indicated by the characteristic peak of sp^2 bonding at around 284.5 eV. In contrast, the oxidation states of the copper matrices in both pristine copper and BM copper-graphene powders exhibit the CuO phase on the surface, particularly displaying a characteristic satellite peak of CuO at 940–945 eV [50], as shown in Fig. 15b. Here, the relative ratio of CuO to copper is further comparable by analyzing the intensity around Cu $2p_{3/2}$ peak. The CuO $2p_{3/2}$ peak appears at around 933.5 eV, while the non-oxidized Cu $2p_{3/2}$ peak is located at around 932.6 eV [50].

Based on this analysis, the relative ratio of CuO to copper in BM copper-graphene is higher than in pristine copper, indicating that indeed BM promotes the oxidation of the copper matrix particles. This ratio peak of CuO to copper continues to rise after the DSC runs in both cases. Therefore, it can be concluded that the DSC runs result in the oxidation of both pristine copper and BM copper-1 wt% graphene powders, and hence this effect should be taken into account.

The influence of oxidation on the ETC and microstructural change in both powders is presented in Fig. 15c-g. The ETC of pristine copper powder increases from 0.43 W/mK to 1 W/mK after eight DSC runs, while that of the copper-graphene composite remains almost unchanged at approximately 0.3 W/mK (see Fig. 15c). To investigate the origin of

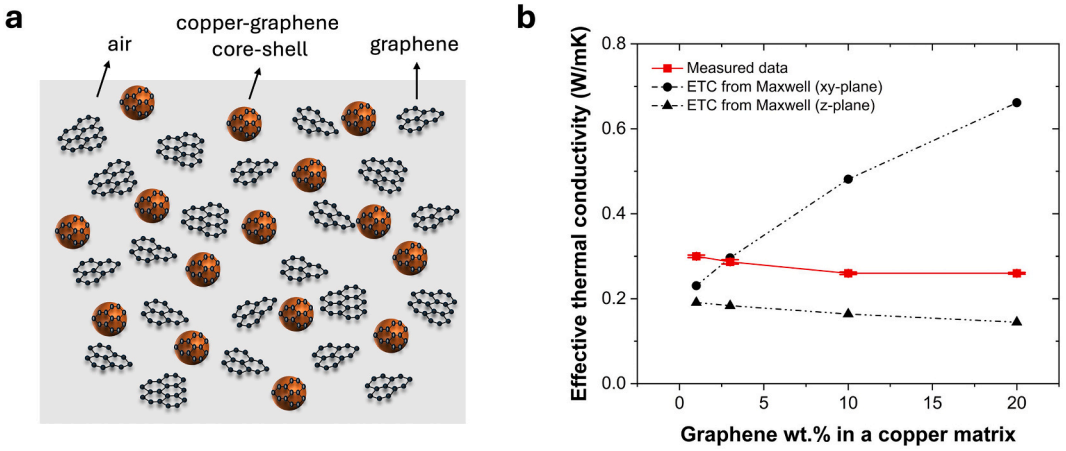

Fig. 14. Effective thermal conductivity predictions of copper-graphene composite powders with higher wt% of graphene (a) Schematic illustrations of two-step homogenization method (b) Effective thermal conductivity of copper-graphene composite powders as a function of the graphene wt%.

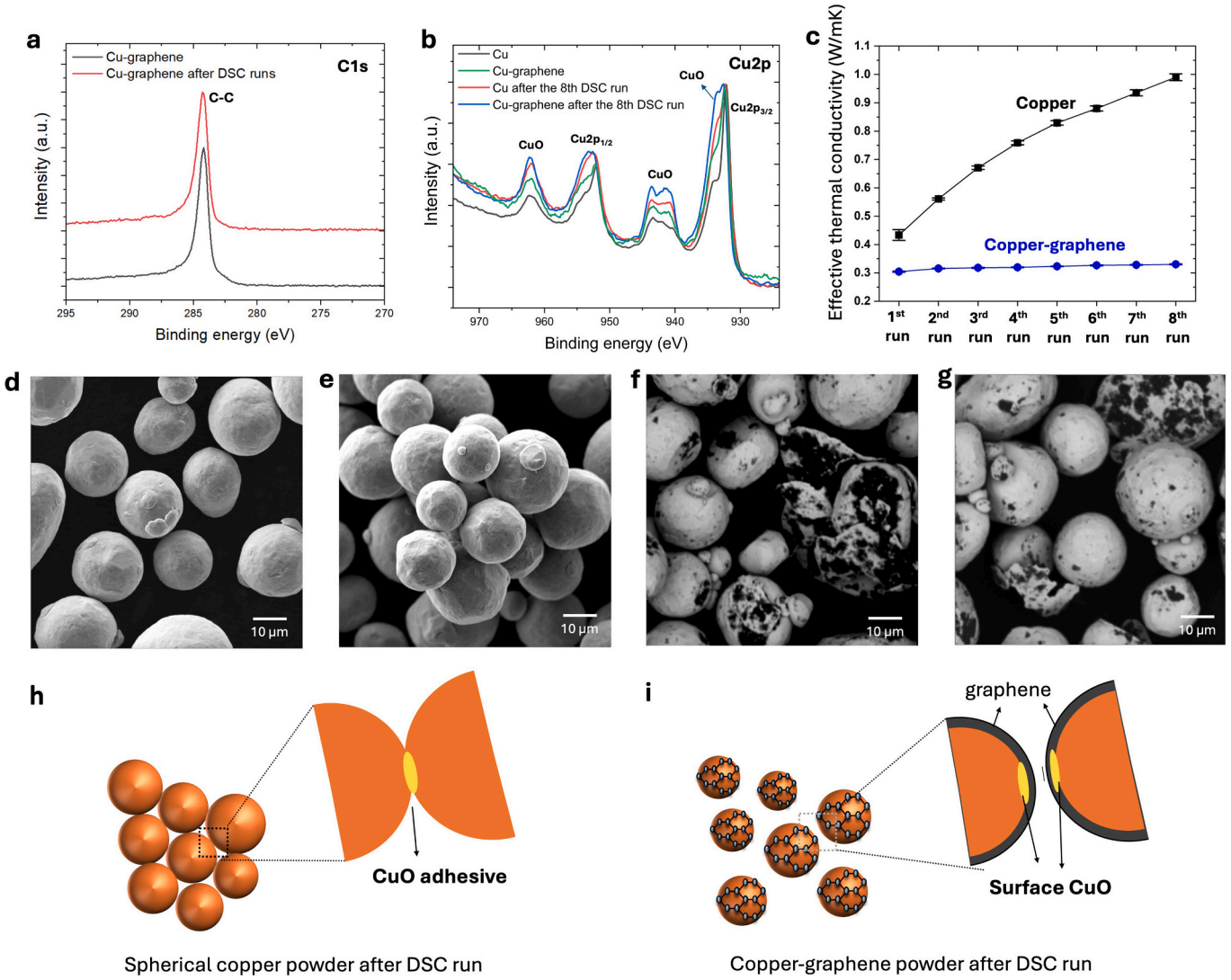

Fig. 15. Effect of oxidation on the microstructural and thermal properties of copper powders: (a-b) XPS characterization of (a) C1s scans of copper with 1 wt% graphene powders before and after DSC runs (b) Cu2p scans of copper and copper with 1 wt% graphene powders before and after DSC runs, (c) Effective thermal conductivity of copper and copper with 1 wt% graphene powders based on the number of DSC runs, (d-g) SEM images (d) before and (e) after DSC runs of copper powders, (f) before and (g) after DSC runs of copper with 1 wt% graphene powders.

these peculiar ETC variations in copper and copper-graphene powders, SEM imaging is performed before and after the DSC runs, as shown in Fig. 15d-g. After the DSC runs, the copper powder exhibits agglomeration between individual particles, whereas the copper-graphene powder shows no signs of such agglomeration. This is likely because the surface CuO layer of spherical copper functions as an adhesive, as revealed by SEM images and illustrated in Fig. 15h. However, this phenomenon is not observed in the copper-graphene powder, as the graphene shell covers the surface of the copper-graphene particle, preventing the agglomeration (see Fig. 15i). When 1 wt% of graphene (3.85 vol%) is fully used to uniformly coat the copper particles, it is expected to form a coating with a 150 nm thickness, which can be thicker if graphene is coated in a patchy manner. Literature sources have reported that the copper oxide-layer thickness is less than 15 nm when heated at 150 °C [69,70]. Thus, the graphene coating completely prevents inter-particle touching of CuO layers due to their thickness variation, thereby preserving the ETC for copper-1 wt% graphene after continuous DSC runs. It should be noted that the graphene shell does not completely prevent the oxidation of copper, as demonstrated by the presence of a CuO peak in Fig. 15b.

As explained by the thermal resistance network model in of Section 4.3, the contact area between individual particles considerably affects the ETC. Therefore, the agglomerated copper particles likely contribute more to the increased ETC, due to the expanded contact radius caused by the CuO adhesive. Hence, this agglomeration effect is hypothesized to be linked to the formation of conductive bridges due to the oxide adhesive, increasing the heat conduction pathways for the copper powder bed.

However, the oxidation of powders should be properly controlled in AM, as oxidation-induced particle agglomeration degrades the flowability [71], and excessive oxides promotes the defect formation during L-PBF [72].

In conclusion, while oxidation of copper powder can enhance the ETC of the powder bed through agglomeration, but it can also negatively affect powder flowability and the quality of the final printed parts. These phenomena are not observed in copper-graphene powder as graphene covers the surface of copper powder, ascribing the decrease in overall ETC to the BM and the addition of graphene.

As discussed, heat conduction in copper, graphene, and copper-graphene composite powder beds is influenced by multiple factors, including BM, graphene addition, and oxidation. To provide an

Table 5
Summary of factors influencing the effective thermal conductivity of powder beds.

Type of powder beds	Factors	Results	Effects on ETCs
Copper	Ball milling	1. Morphology change 2. Reduction in packing density	Decrease
Graphene	Ball milling	Increase in aspect ratio (thickness to lateral size)	Decrease
Copper-graphene	Graphene addition	Decrease in contact radius	Decrease
Oxidized copper	Oxidation	Increase in contact radius	Increase
Oxidized copper-graphene	Oxidation	No change	No difference

overview, individual factors that may affect the ETC of powder beds are listed in Table 5, along with their results in microstructural and chemical compositional features.

Overall, BM results in a decrease in ETC of any type of powder beds, which is attributed to the microstructural change. This includes changes in packing density, morphological transition, and particle aspect ratio after BM times of 12 h or more. The addition of graphene to the copper powder also reduces the ETC, as the graphene coating reduces the particle-to-particle contact radius and particle contact conduction. Lastly, the oxidation of copper powder leads to agglomeration, which can have a positive effect on the ETC, but negative impact on flowability and the parts quality. This effect arises from an increased contact radius between particles due to oxide acting as adhesive, leading to the formation of better heat-conduction pathways. This effect is however not observed as strongly in copper-graphene powders.

As reviewed in the introduction and Section 2, the thermal properties of powder beds are critical factors influencing the heat dissipation rate in powder-bed-based AM processes, such as PBF [1,2]. Consequently, process parameter in AM can be significantly affected by the ETC values in the powder bed, as higher ETC values correspond to higher heat dissipation. In other words, characterizing the ETC strongly assists in optimizing process parameters and ensuring the quality of printed parts. To the best of our knowledge, there have been no studies to date on the thermal characterization of copper-graphene composite powders, particularly regarding their heat conduction in complex metal-2D composite powder beds.

5. Conclusions

In this work, the characterization of the ETC of copper-graphene composite powders produced by BM is presented. This includes an interpretation of the observed thermal behavior using well-established thermal models. The ETC values provided in this study facilitates the application of 2DMMC composite powders, such as copper-graphene powders, in the field of heat transfer devices, such as heat sink and heat exchanger fabricated using AM technologies. Furthermore, the reported thermal data will support numerical modeling of AM processes by offering accurate ETC values for copper-graphene composite powder beds.

The thermal properties of copper, graphene, and copper-graphene powders produced by BM are individually characterized using the extended DSC method, alongside extensive microstructure analysis. Based on these thermal characterizations, the following conclusions are drawn:

1. An extended DSC method is used based on steady-state measurement, with an error of 3.6 % and a repeatability variations of 5 %, making it particularly suitable for the thermal characterization of powder beds.
2. The ETC of powder beds has been characterized and compared with predictions from thermal models, including the Maxwell-Garnett approximation model and the thermal resistance network model. As a result, heat conduction mechanisms in powder beds, including fluid-phase conduction and contact conduction are clarified.
3. BM results in a decrease in ETC for both copper and graphene due to the change in morphology. Copper particles experience a morphological change from spherical to polyhedral to flaky shapes. Graphene particles undergo alterations in the particle aspect ratio. Overall, the ETC of copper powder decreases by 45 %, while that of graphene powder is reduced by 70 % after 24 h of BM.
4. The addition of graphene onto the copper powder decreases the ETC, due to the reduced contact radius, at 1 wt% of graphene addition. At higher wt% of graphene (3 wt%, 10 wt% and 20 wt%) addition, the ETC of powder decreases by 40 % compared to the pristine copper powder. This is because heat is mainly conducted through the fluid phase, due to the reduced inter-particle contact from graphene.
5. Oxidation of copper powder increases the ETC from 0.43 W/mK to 1 W/mK. This is attributed to enhancements of particle-to-particle contact heat conduction by CuO adhesive-induced particle agglomeration. However, copper-graphene powders do not exhibit such strong agglomeration and hence increase in ETC.

Overall, the ETC of copper-graphene composite powder bed differs from its intrinsic thermal conductivity. This is due to the generally poor heat conduction of the fluid phase (air in this case) and variation in heat conduction through particle-to-particle contacts caused by morphology modifications. Hence, in future studies, the intrinsic thermal conductivity of copper-graphene will be investigated to determine the optimal wt% of graphene for conductivity enhancement; e.g. cold or hot-pressed parts can be a benchmark system that enables the measurement of intrinsic thermal conductivity, eliminating the complex effects of the powder bed, prior to studying the thermal properties of AM copper-graphene parts. Furthermore, another future study investigating the impact of ETC variation in copper-graphene on the AM process window, such as resulting laser power and scan speed is suggested, for AM process optimization.

CRediT authorship contribution statement

Hyunjong Lee: Writing – original draft, Visualization, Investigation, Formal analysis, Conceptualization. **Davoud Jafari:** Writing – review & editing, Supervision, Conceptualization. **Apostolos Koutsioukis:** Methodology, Formal analysis, Conceptualization. **Valeria Nicolosi:** Writing – review & editing, Conceptualization. **Bernard.J. Geurts:** Writing – review & editing, Supervision, Conceptualization. **Wessel W. Wits:** Writing – review & editing, Supervision, Project administration, Conceptualization.

Declaration of competing interest

The authors declare that they have no known competing financial interests or personal relationships that could have appeared to influence the work reported in this paper.

Acknowledgment

This work was supported by ThermoDust, a project funded under grant agreement No. 101046835 from the European Union's Horizon and Europe research programme.

Appendix A. Supplementary data

Supplementary data to this article can be found online at https://doi.org/10.1016/j.powtec.2025.121423.

Data availability

No data was used for the research described in the article.

References

[1] Y. Zhao, Y. Koizumi, K. Aoyagi, K. Yamanaka, A. Chiba, Thermal properties of powder beds in energy absorption and heat transfer during additive manufacturing with electron beam, Powder Technol. 381 (2021) 44–54.

[2] A. Hofmann, A. Huber, A. Mahr, C. Bay, F. Döpper, Influence of the effective thermal conductivity of the powder bed on the properties of overhanging areas in laser-based powder bed fusion of Ti-6Al-4V, Proc. CIRP 111 (2022) 138–143.

[3] W.W. Wits, C. de Vos, M. Montero-Sistiaga, M. de Smit, Laser powder bed fusion process parameters for the fabrication of unsupported overhang structures of metamaterial lattices, CIRP Ann. 74 (2025) 309–313.

[4] C. Li, M.F. Gouge, E.R. Denlinger, J.E. Irwin, P. Michaleris, Estimation of part-to-powder heat losses as surface convection in laser powder bed fusion, Addit. Manuf. 26 (2019) 258–269.

[5] D.A. De Moraes, A. Czekanski, Parametric thermal FE analysis on the laser power input and powder effective thermal conductivity during selective laser melting of SS304L, J. Manufact. Mater. Proc. 2 (2018) 47.

[6] W.W. Wits, R. Bruins, L. Terpstra, R.A. Huls, H.J.M. Geijselaers, Single scan vector prediction in selective laser melting, Addit. Manuf. 9 (2016) 1–6.

[7] M. Rombouts, L. Froyen, A. Gusarov, E. Bentefour, C. Glorieux, Photopyroelectric measurement of thermal conductivity of metallic powders, J. Appl. Phys. 97 (2005).

[8] M. Liu, L.N.S. Chiu, H. Shen, X. Fang, Z. Tao, A. Huang, C. Davies, X. Wu, W. Yan, Effective thermal conductivities of metal powders for additive manufacturing, Powder Technol. 401 (2022) 117323.

[9] L.C. Wei, L.E. Ehrlich, M.J. Powell-Palm, C. Montgomery, J. Beuth, J.A. Malen, Thermal conductivity of metal powders for powder bed additive manufacturing, Addit. Manuf. 21 (2018) 201–208.

[10] C.P. Camirand, Measurement of thermal conductivity by differential scanning calorimetry, Thermochim. Acta 417 (2004) 1–4.

[11] S. Kandhasamy, A. Støre, G.M. Haarberg, S. Kjelstrup, A. Solheim, Thermal conductivity of molten carbonates with dispersed solid oxide from differential scanning calorimetry, Materials 12 (2019) 1486.

[12] H. Lee, A. Koutsioukis, D. Jafari, B.J. Geurts, W.W. Wits, Measurement of effective thermal conductivity of composite powders of 2D materials and metals for additive manufacturing, Journal of Physics: Conference Series, IOP Publishing, 2024, pp. 012186.

[13] I. Ovid'Ko, Metal-graphene nanocomposites with enhanced mechanical properties: a review, Rev. Adv. Mater. Sci. 38 (2014).

[14] S. Ali, F. Ahmad, P.S.M.M. Yusoff, N. Muhamad, E. Oñate, M.R. Raza, K. Malik, A review of graphene reinforced cu matrix composites for thermal management of smart electronics, Compos. A: Appl. Sci. Manuf. 144 (2021).

[15] K. Chu, F. Wang, X.-H. Wang, D.-J. Huang, Anisotropic mechanical properties of graphene/copper composites with aligned graphene, Mater. Sci. Eng. A 713 (2018) 269–277.

[16] H. Lee, A.A. Lordejani, L. van Goor, A. Jurov, A. Koutsioukis, S. Ruan, N. M. Santhosh, F. Zarei, C. Barreneche, U. Cvelbar, S. Dosta, B.J. Geurts, M. Guagliano, D. Jafari, V. Nicolosi, S. Yin, J. Zavašnik, S. Bagherifard, R. Lupoi, W.W. Wits, Review on properties, physics, and fabrication of two-dimensional material-based metal-matrix composites (2DMMCs) for heat transfer systems, Renew. Sust. Energ. Rev. 217 (2025) 115700.

[17] A.A. Balandin, S. Ghosh, W. Bao, I. Calizo, D. Teweldebrhan, F. Miao, C.N. Lau, Superior thermal conductivity of single-layer graphene, Nano Lett. 8 (2008) 902–907.

[18] K. Chu, X.-H. Wang, F. Wang, Y.-B. Li, D.-J. Huang, H. Liu, W.-L. Ma, F.-X. Liu, H. Zhang, Largely enhanced thermal conductivity of graphene/copper composites with highly aligned graphene network, Carbon 127 (2018) 102–112.

[19] J. Li, P. Zhang, H. He, B. Shi, Enhanced the thermal conductivity of flexible copper foil by introducing graphene, Mater. Des. 187 (2020).

[20] X. Wang, Y. Liu, X. Wang, Y. Wang, T. Lai, G. Ren, Tuning thermal expansion coefficient of copper-multilayer graphene thermal management materials through tailoring interfacial microstructure, J. Alloys Compd. 862 (2021) 158709.

[21] I. Gibson, D.W. Rosen, B. Stucker, M. Khorasani, D. Rosen, B. Stucker, M. Khorasani, Additive Manufacturing Technologies, Springer, 2021.

[22] Y. Li, Z. Feng, L. Huang, K. Essa, E. Bilotti, H. Zhang, T. Peijs, L. Hao, Additive manufacturing high performance graphene-based composites: a review, Compos. A: Appl. Sci. Manuf. 124 (2019) 105483.

[23] M. Abedi, D. Moskovskikh, V. Romanovski, D. Ozherelkov, A. Gromov, Unlocking the potential of graphene-reinforced AlSi10Mg nanocomposites in laser powder bed fusion: a comprehensive review, J. Alloys Compd. 978 (2024) 173441.

[24] M. Dong, W. Zhou, K. Kamata, N. Nomura, Microstructure and mechanical property of graphene oxide/AlSi10Mg composites fabricated by laser additive manufacturing, Mater. Charact. 170 (2020) 110678.

[25] S. Chowdhury, N. Yadaiah, C. Prakash, S. Ramakrishna, S. Dixit, L.R. Gupta, D. Buddhi, Laser powder bed fusion: a state-of-the-art review of the technology, materials, properties & defects, and numerical modelling, J. Mater. Res. Technol. 20 (2022) 2109–2172.

[26] S. Tiden, M. Taher, M. Vennstrom, U. Jansson, Additive manufacturing of cu using graphene-oxide-treated powder, Materials (Basel) 16 (2023).

[27] F. Calignano, M. Pavese, A. Saboori, M. Galati, L. Iuliano, Additive manufacturing of copper with a single mode IR fiber laser, Proc. CIRP 118 (2023) 649–653.

[28] T. Prasad Yadav, R. Manohar Yadav, D. Pratap Singh, Mechanical milling: a top down approach for the synthesis of nanomaterials and nanocomposites, Nanosci. Nanotechnol. 2 (2012) 22–48.

[29] A. Naseer, F. Ahmad, M. Aslam, B.H. Guan, W.S.W. Harun, N. Muhamad, M. R. Raza, R.M. German, A review of processing techniques for graphene-reinforced metal matrix composites, Mater. Manuf. Process. 34 (2019) 957–985.

[30] M. Yi, Z. Shen, A review on mechanical exfoliation for the scalable production of graphene, J Mater Chem A 3 (2015) 11700–11715.

[31] O.A. Tertuliano, P.J. DePond, D. Doan, M.J. Matthews, X.W. Gu, W. Cai, A.J. Lew, Nanoparticle-enhanced absorptivity of copper during laser powder bed fusion, Addit. Manuf. 51 (2022).

[32] F. Chu, E. Li, H. Shen, Z. Chen, Y. Li, H. Liu, S. Min, X. Tian, K. Zhang, Z. Zhou, R. Zou, J. Hou, X. Wu, A. Huang, Influence of powder size on defect generation in laser powder bed fusion of AlSi10Mg alloy, J. Manuf. Process. 94 (2023) 183–195.

[33] A. Mussatto, R. Groarke, A. O'Neill, M.A. Obeidi, Y. Delaure, D. Brabazon, Influences of powder morphology and spreading parameters on the powder bed topography uniformity in powder bed fusion metal additive manufacturing, Addit. Manuf. 38 (2021).

[34] K. Riener, N. Albrecht, S. Ziegelmeier, R. Ramakrishnan, L. Haferkamp, A. B. Spierings, G.J. Leichtfried, Influence of particle size distribution and morphology on the properties of the powder feedstock as well as of AlSi10Mg parts produced by laser powder bed fusion (LPBF), Addit. Manuf. 34 (2020).

[35] J. Gan, Z. Zhou, A. Yu, Effect of particle shape and size on effective thermal conductivity of packed beds, Powder Technol. 311 (2017) 157–166.

[36] J. Lee, T.S. Yun, S.-U. Choi, The effect of particle size on thermal conduction in granular mixtures, Materials 8 (2015) 3975–3991.

[37] A.K. Mishra, A. Kumar, Effect of different powder bed thermal conductivity models on the melt Pool characteristics and solidification parameters during laser powder bed fusion of Ti6Al4V, Trans. Indian Inst. Metals 77 (2024) 2971–2975.

[38] W. Li, D. Li, Q. Fu, C. Pan, Conductive enhancement of copper/graphene composites based on high-quality graphene, RSC Adv. 5 (2015) 80428–80433.

[39] Y. Cui, L. Wang, B. Li, G. Cao, W. Fei, Effect of ball milling on the defeat of few-layer graphene and properties of copper matrix composites, Acta Metall. Siin. (Engl. Lett.) 27 (2014) 937–943.

[40] Y. Takashimizu, M. Iiyoshi, New parameter of roundness R: circularity corrected by aspect ratio, Prog. Earth Planet Sci. 3 (2016) 2.

[41] W. Fei, G. Narsilio, Impact of three-dimensional Sphericity and roundness on coordination number, J. Geotech. Geoenviron. Eng. 146 (2020) 06020025.

[42] D.C. del Rio, D.J. Jensen, N.S. Tiedje, S. Fæster, T. Yu, Factors affecting particle characterization of powders used in additive manufacturing, Powder Technol. 434 (2024) 119324.

[43] J. Lindblad, I. Nyström, Surface area estimation of digitized 3D objects using local computations, in: Discrete Geometry for Computer Imagery: 10th International Conference, DGCI 2002 Bordeaux, France, April 3–5, 2002 Proceedings vol. 10, Springer, 2002, pp. 267–278.

[44] U. Ali, Y. Mahmoodkhani, S. Imani Shahabad, R. Esmaeilizadeh, F. Liravi, E. Sheydaeian, K.Y. Huang, E. Marzbanrad, M. Vlasea, E. Toyserkani, On the measurement of relative powder-bed compaction density in powder-bed additive manufacturing processes, Mater. Des. 155 (2018) 495–501.

[45] F. Ahsan, J. Razmi, L. Ladani, Experimental measurement of thermal diffusivity, conductivity and specific heat capacity of metallic powders at room and high temperatures, Powder Technol. 374 (2020) 648–657.

[46] G. Della Gatta, M.J. Richardson, S.M. Sarge, S. Stølen, Standards, calibration, and guidelines in microcalorimetry. Part 2. Calibration standards for differential scanning calorimetry*(IUPAC technical report), Pure Appl. Chem. 78 (2006) 1455–1476.

[47] A. Berger, U. Ziesing, S. Benito, S. Weber, Experimental determination of the high-temperature thermal conductivity of steel powders, Powder Technol. 431 (2024) 119022.

[48] A. Movahedi-Rad, S.S. Pelaseyed, M. Attarian, R. Shokrallahzadeh, Oxidation behavior of AISI 321, AISI 316, and AISI 409 stainless steels: kinetic, thermodynamic, and diffusion studies, J. Mater. Res. 31 (2016) 2088–2096.

[49] W. Zhao, Y. Yang, Z. Bao, D. Yan, Z. Zhu, Methods for measuring the effective thermal conductivity of metal hydride beds: a review, Int. J. Hydrog. Energy 45 (2020) 6680–6700.

[50] S. Poulston, P. Parlett, P. Stone, M. Bowker, Surface oxidation and reduction of CuO and Cu2O studied using XPS and XAES, surface and interface analysis: An International Journal devoted to the development and application of techniques for the analysis of surfaces, interfaces and thin films 24 (1996) 811–820.

[51] A. Bor, B. Jargalsaikhan, K. Uranchimeg, J. Lee, H. Choi, Particle morphology control of metal powder with various experimental conditions using ball milling, Powder Technol. 394 (2021) 181–190.

[52] J.Y. Huang, Y.K. Wu, H.Q. Ye, Ball milling of ductile metals, Mater. Sci. Eng. A 199 (1995) 165–172.

[53] Y.X. Liang, Z.M. Wu, E.G. Fu, J.L. Du, P.P. Wang, Y.B. Zhao, Y.H. Qiu, Z.Y. Hu, Refinement process and mechanisms of tungsten powder by high energy ball milling, Int. J. Refract. Met. Hard Mater. 67 (2017) 1–8.

[54] R.A. Raimundo, F.A. Costa, M.A. Morales, A.G.P. Silva, U.U. Gomes, Effect of the high energy milling on the microstructure of cu-20%WC composite powders prepared with recycled WC, Int. J. Refract. Met. Hard Mater. 90 (2020) 105223.

[55] J.C. Maxwell, A treatise on electricity and magnetism, Clarendon Press Google Schola 2 (1873) 3408–3425.

[56] N.M. Figueiredo, A. Cavaleiro, Dielectric properties of shape-distributed ellipsoidal particle systems, Plasmonics 15 (2020) 379–397.

[57] K.L. Johnson, Contact Mechanics, Cambridge University Press, 1987.
[58] S.E. Wood, A mechanistic model for the thermal conductivity of planetary regolith: 1. The effects of particle shape, composition, cohesion, and compression at depth, Icarus 352 (2020) 113964.
[59] L.B. Freund, S. Suresh, Thin Film Materials: Stress, Defect Formation and Surface Evolution, Cambridge University Press, 2004.
[60] T.A. Ring, P. Feeney, D. Boldridge, J. Kasthurirangan, S. Li, J.A. Dirksen, Brittle and ductile fracture mechanics analysis of surface damage caused during CMP, J. Electrochem. Soc. 154 (2007) H239.
[61] V.A. Markel, Introduction to the Maxwell Garnett approximation: tutorial, J. Opt. Soc. Am. A 33 (2016) 1244–1256.
[62] E. Pop, V. Varshney, A.K. Roy, Thermal properties of graphene: fundamentals and applications, MRS Bull. 37 (2012) 1273–1281.
[63] A.A. Balandin, Thermal properties of graphene and nanostructured carbon materials, Nat. Mater. 10 (2011) 569–581.
[64] H. Malekpour, P. Ramnani, S. Srinivasan, G. Balasubramanian, D.L. Nika, A. Mulchandani, R.K. Lake, A.A. Balandin, Thermal conductivity of graphene with defects induced by electron beam irradiation, Nanoscale 8 (2016) 14608–14616.
[65] C. Lanzerstorfer, Flow properties of additive manufacturing metal powders: influencing parameters and wall friction reduction by diamond-like carbon coating, Int. J. Adv. Manuf. Technol. 136 (2025) 5427–5435.
[66] A. Gusarov, E. Kovalev, Model of thermal conductivity in powder beds, Phys. Rev. B—Condens. Matt. Mater. Phys. 80 (2009) 024202.
[67] U.K. Chettiar, N. Engheta, Internal homogenization: effective permittivity of a coated sphere, Opt. Express 20 (2012) 22976–22986.
[68] A. Politano, A.R. Marino, D. Campi, D. Farías, R. Miranda, G. Chiarello, Elastic properties of a macroscopic graphene sample from phonon dispersion measurements, Carbon 50 (2012) 4903–4910.
[69] S.R. Esa, R. Yahya, A. Hassan, G. Omar, Nano-scale copper oxidation on leadframe surface, Ionics 23 (2017) 319–329.
[70] C.-H. Tseng, K.N. Tu, C. Chen, Comparison of oxidation in uni-directionally and randomly oriented cu films for low temperature Cu-to-Cu direct bonding, Sci. Rep. 8 (2018) 10671.
[71] J.H. Tan, W.L.E. Wong, K.W. Dalgarno, An overview of powder granulometry on feedstock and part performance in the selective laser melting process, Addit. Manuf. 18 (2017) 228–255.
[72] C.L.A. Leung, S. Marussi, M. Towrie, R.C. Atwood, P.J. Withers, P.D. Lee, The effect of powder oxidation on defect formation in laser additive manufacturing, Acta Mater. 166 (2019) 294–305.